Applied Computational Electromagnetics Society

March 2004

APPLIED COMPUTATIONAL ELECTROMAGNETICS SOCIETY (ACES)

NEWSLETTER

Vol. 19 No. 1   March 2004

TABLE OF CONTENTS

PERMANENT STANDING COMMITTEES OF ACES, INC.

COMMITTEE	CHAIRMAN	ADDRESS
NOMINATION & ELECTIONS	Rene Allard	Penn State University PO Box 30 State College, PA 16804-0030 rja5@psu.edu
FINANCE	Andrew Peterson	Georgia Institute of Technology School of ECE Atlanta, GA 30332-0250 peterson@ece.gatech.edu
PUBLICATIONS	Atef Elsherbeni	EE Department, Anderson Hall University of Mississippi University, MS 38677 atef@olemiss.edu
CONFERENCE	Osama Mohammed	Florida International University ECE Department Miami, FL 33174 mohammed@fiu.edu
AWARDS	Ray Perez	Martin Marietta Astronautics MS 58700, PO Box 179 Denver, CO 80201 ray.j.perez@lmco.com

MEMBERSHIP ACTIVITY COMMITTEES OF ACES, INC.

COMMITTEE	ADDRESS	CHAIRMAN
SOFTWARE VALIDATION	Bruce Archambeault	IBM 3039 Cornwallis Road, PO Box 12195; Dept.18DA B306 Research Triangle Park, NC 27709 barch@us.ibm.com
HISTORICAL	Robert Bevensee	BOMA Enterprises PO Box 812 Alamo, CA 94507-0812 rmbevensee@cs.com
CONSTITUTION & BYLAWS	Leo Kempel	2120 Engineering Building Michigan State University East Lansing, MI 48824 kempel@egr.msu.edu
MEMBERSHIP & COMMUNICATIONS	Vicente Rodriguez	ETS-LINDGREN L.P. 1301 Arrow Point Drive Cedar Park, TX 78613 rodriguez@ieee.org
INDUSTRIAL RELATIONS	Andy Drozd	ANDRO Consulting Services PO Box 543 Rome, NY 13442-0543 andro1@aol.com

PRESIDENT'S POST

The past two years have been very exciting for ACES and its membership. I am pleased to report to you on several activities and accomplishments that have propelled our society to be of more value to its members.

- Membership fees have now been streamlined reduced and have become very reasonable at $35.00 annually. This is lowest of many if not all of the technical societies. The conference registration fees have remained low with more technical and social events added.
- In an effort to increase membership services, conference proceedings and journal archives are available on CD for ACES members and nonmembers. The society is moving more and more towards complete electronic publications and services. We have enhanced membership communications and placed more information on the website.
- The conference committee is working hard to identify sites and groups who will agree to organize the conference for the next five years. Since our annual conference is the main source of funding, this long-range plan is very important to ensure the long-term viability of the society's finances. Now, the ACES annual conference venue can move around the country or even around the world allowing more groups to organize the conference and help increase the financial viability of the society.
- A new feature for the annual conference now is that authors of accepted papers will have the option to submit an extended version of their papers for peer review and possible publication in special issues of the ACES Journal. *And most importantly,*
- It is with great pleasure that I inform you that the Applied Computational Electromagnetic Society Journal has officially been added to the *Science Citation Index Expanded*, the *Research Alert* as well as to *Current Contents/Engineering, Computing & Technology*. This indeed is a new and an important milestone for all of us at ACES. This will enhance the archival value of our Society's Journal and increase our circulation and referral to ACES Journal articles in the scientific community. This inclusion has officially started with the 2003 issues of the Journal. We are all proud of this accomplishment.

The Journal is a highly refereed publication and is published regularly three times annually (March, July and November) in addition to special issues. I encourage you to submit your articles for review and possible publication in the ACES Journal. It is possible that with increased interest that the Journal may become more frequent with additional regular issues. My most sincere thanks and congratulations to all who have led this effort to achieve this milestone; Andy Peterson, Atef Elsherbeni, Dick Adler, many others and certainly all of you who have been contributing to the Journal. You can visit the Journal Website at http://aces.ee.olemiss.edu/acesjournal.asp. All submissions and the review processes for the journal are done online and I am sure you will all want the ACES Journal to achieve its highest impact with your contributions and support.

Preparations for this year's ACES annual conference are in full swing. It will be held April 19-23, 2004. This year's conference will be held in Syracuse, New York. The conference venue is the Sheraton Hotel on the Campus of Syracuse University. The conference is our society's main event and its continued success is everyone's business. We look forward to the support of everyone who can help make the 2004 conference in Syracuse a great event. The conference this year features 160 presentations in addition to several tutorials and company exhibits. The technical and social programs promise to be exciting. This

year we will continue the feature started last year which would allow authors of accepted papers to have the option to submit an extended version of their papers for review and publication in special issues of the ACES Journal. This feature created three special issues of the Journal during the past year and will continue to give authors the chance to have their papers peer reviewed and possibly published in the ACES Journal.

The ACES annual conference is a highly influential outlet for promoting awareness of recent technical contributions to the advancement of computational electromagnetics. Attendance of ACES members as well as nonmembers from throughout the world is encouraged and welcomed. The Board of Directors invites every ACES member to participate and encourage their colleagues to submit and present papers at the annual conference and/or organize a session, tutorial or participate in the vendor exhibit.

The overall future of ACES is very bright and the society will continue to be valuable to its members. The key for us is to utilize the opportunities inherent in the dramatic changes in our world and our technology. Relevance to our members with products and services as well as choices will increase membership and enhance attendance at the annual symposium. We need to do more:

- The society seeks the efforts of its overseas BoD members from Europe and Asia to help in the creation of ACES chapters overseas and encourage basic and student membership. Now, the membership fees are very reasonable and attractive.
- The ACES web site has become an important tool in delivering membership services and publications. We look forward to its continued enhancements and increased full services such as membership renewals and publications. The ACES web site will be the main source for delivering almost all of the membership services as well as conferences, publications and administrative activities.
- We look forward to everyone's help in increasing the society membership to the level of 2000 members in the near future. This will be in concert with the quality and high level of our publications as well as our mission.

I will continue to promote ACES on all fronts and increase communication and cooperation with other organizations. We must all work together if we are to grow, prosper and reach our goals.

Please feel free to contact me with your comments and suggestions.

Osama Mohammed
President
Applied Computational Electromagnetic Society
Telephone: +1 305 348-3040
E-mail: mohammed@fiu.edu

CEM NEWS FROM EUROPE

MESSAGE FROM THE EUROPEAN NEWS EDITOR

This issue sees a change in the editorial desk for this column. Our long term news editor, Pat Foster , has hung up her word processor after many years undertaking this role. I would like to thank Pat for her exemplary effort .

For the future, the intention is use this space for both news and direct technical interest . The format is a short report on matters of interest to ACES and the CEM community followed by a 'spotlight' feature on different institutions working throughout Europe. The spotlight gives a forum for European CEM workers to highlight their work ,with the hope that this will encourage contact between those with like minded issues across the ACES community .

I would like to thank all the contributors to this issue for their support. I would also welcome comments, suggestions and contributions from all colleagues, especially those throughout Europe.

<div align="right">

Tony Brown, a.brown@umist.ac.uk
Professor of Communication Engineering, UMIST,UK
</div>

GENERAL NEWS

ACES UK Chapter is cosponsoring two events headed by the Institute of Electrical Engineers (IEE) and of interest to the CEM community.

The first is entitled 'Validation of Computational Electromagnetics' to be held Monday 29th March 2004 at BAESystems Ltd, Farnborough UK (www.iee.org/events/validation.cfm) . The second event is the next in the IEE's series of conferences on Computational Electromagnetics, to be held 19th to 22nd April 2004 at Stratford-upon-Avon , UK (http://conferences.iee.org/CEM).These are had at approximately 3 year intervals.

SPOTLIGHT FEATURE

This issue we are spotlighting the University of Manchester, England. As a background , the University is currently restructured and in Oct 2004 will become the largest in the UK. CEM is used widely throughout communications, microwave and power engineering departments. Space dictates we can only highlight a few of the many programs underway. Interested readers are invited to contact the contributors directly.

Analysis of Ferrite Components(Andy Gibson, a.gibson@umist.ac.uk)

Of particular importance in many applications non-reciprocal ferrite components present particular problems for analysis, particularly for high power applications were temperature profile is of considerable concern. Bias field selection, nonlinear losses, partial magnetization and the temperature sensitivity of ferrite materials pose significant problems for realistic device modeling. New numerical techniques, which model non-linear loss and coupled thermal/electromagnetic behavior are being developed at UMIST to aid the innovation process.

A finite element magnetostatic solver is used to solve the nonlinear Poisson equation in terms of the magnetic vector potential. The flux density, magnetic field intensity and magnetization are all evaluated using the magnetic potential and the material magnetization curve. These quantities are used to evaluate the microwave tensor permeability throughout the ferrite. The tensor permeability is substituted into a formulation written in terms of the transverse electric and magnetic microwave fields. Using Bossivit type edge elements an eigenvalue solver calculates the complex propagation constant and field components as a function of the material tensor permeability entries and signal frequency.

The microwave field solution is used to calculate the dissipated power and this acts as the source for the steady-state heat conduction equation. The thermal solution is obtained using an electrostatic type finite element solver. In the iterative process the intermediate solution is compared with the previous solution and a converged solution was reached when the temperature difference was less than 0.5°C. This was found to occur after two or three iterations.

FDTD analysis of Ultra Wide Band propagation in Lossy Media (Fumie Costen

f.costen@cs.man.ac.uk)

Our research focuses upon the use of the frequency dependent finite difference time domain method (FD-FDTD) with consideration of the conductive loss to give us the waveform of UltraWideBand pulses in a lossy media. From the viewpoint of the computation of electromagnetics using FD-FDTD, memory and computational load reductions are the major concerns. In many situations, the voxel size required is much finer than the minimum allowed by FDTD calculation accuracy. In addition, the time step of the conventional explicit FDTD scheme has to satisfy the Courant-Friedrich-Levy (CFL) condition to ensure stability .Thus, the maximum time step is limited by voxel size. Obviously, this over time-sampling leads to an increase in the
signal processing time. To eliminate the constraint of the CFL condition, a scheme called alternating-direction implicit (ADI) FDTD has been proposed.

The Debye model is often applied in FDTD schemes to incorporate frequency dependent material. Our work is novel in its application of the Debye model to ADI-FDTD to construct a frequency dependent ADI-FDTD including conductive loss. Our current problem is asymmetry in the implementation of this novel scheme. A tridiagonal matrix inversion is currently involved in the algorithm in the same way as ADI-FDTD. However, this matrix inversion, in our case to calculate the electric flux field (electric field values in the original ADI-FDTD) causes asymmetry. The symbolic expression of the result of matrix inversion does not match what theoretically happens in wave propagation, mainly because the calculation area is not infinite. Even when the symbolic expression shows symmetry, the numerical outcome is not symmetry due to rounding errors in the matrix inversion. The ideal solution for this would be an alternative method to avoid this matrix inversion. This issue is currently being investigated.

Ultra Wide Band Propagation using ray tracing techniques in the time domain (Yongwei

Zhang yw.zhang@postgrad.umist.ac.uk, Tony Brown a.brown@umist.ac.uk)

The objective of our research is analyze the performance of a UWB system in a complex, potentially multi-room environment. The prime focus is the channel delay which in practice is a key parameter heavily influenced by multipath in the environment. A ray tracing technique has been adopted due to the size of the problem space. This is used with a impulse function source to develop a time domain transfer function for the problem so that the received signal from a complex, measured, input signal can be readily constructed via a complex convolution integral.
In a multi-room environment many hundreds of rays must potentially be traced . An algorithm has been developed to minimize the run time. So far the results of the program are extremely encouraging even for a multi-room scenario. The long term goal of the research is to provide a flexible tool which will give a physical insight into the propagation mechanisms and aid our research on UWB antennas and components . Our emphasis therefore is on computational speed within acceptable accuracy, rather than attempting a fully deterministic model. By linking this simulation with conventional TLM analysis of antenna and rf components, we aim to produce a end to end UWB link simulator for these complex environments.

Use of FE Software In High Voltage Group, UMIST (Ian Cotton ian.cotton@umist.ac.uk**)**
The electrostatic package of OPERA 3-D is used for a range of research tasks in our group. It is mainly used to obtain electric field distributions of basic geometries such as the rod-plane and rod-rod gaps, and more complex geometries involving profiled insulators, cable with clips and the fin of a wind turbine to name but a few. This has made it possible to determine inception fields and relevant field distributions for the study of partial discharges, streamer propagation and lightning attachment. In addition, energy calculations are obtained from this software and associated capacitance values estimated for the various geometries mentioned.

NOTE: The Financial Report (below) is tentative and is subject to further review and revision.

2003 FINANCIAL REPORT

ASSETS

BANK ACCOUNTS	1 JAN 2003	31 DEC 2003
MAIN CHECKING	9,431	16,377
EDITOR CHECKING	3,325	3,334
SECRETARY CHECKING	6,458	6255
SAVINGS	111	111
HIGH RATE SAVINGS	37,320	23,242
CREDIT CARD	1,587	10,202
CD #1	14,088	14,523
CD #2	13,968	14,204
CD #3	14,071	14,401
CD #4	13,982	14,413
TOTAL ASSETS	$114,342	$117,023

LIABILITIES: $0

NET WORTH   31 December 2002: $117,023

INCOME

Conference	59,300	
Short Courses	4,560	
Publications	530	
Membership	22,653	
Interest & misc.	2,259	
TOTAL	$89,302	

EXPENSE

Conference	48,666	
Short Courses	3,149	
Publications	12,615	
Services (Legal, Taxes)	1,511	
Postage	6,518	
Supplies & misc.	14,125	
TOTAL	$86,584	

NET INCREASE for 2003 was $2,718

In 2002, the net operating loss was $22,637. In 2003 our net operating profit was $2,718, an improvement of $25,355.   Our current net worth, $117,203, has increased by 2.3% from last year.

Allen Glisson
Treasurer

THE APPLIED COMPUTATIONAL ELECTROMAGNETICS SOCIETY, INC.

NOTICE OF THE ANNUAL BUSINESS MEETING

Notice is hereby given that the annual business meeting of the Applied Computational Electromagnetics Society, Inc. will be held on Monday 19 April 2004, at the Sheraton Syracuse University Hotel, & Conference Center, Syracuse, NY. The meeting is scheduled to begin at 7:55 AM EDT for purposes of:
1.   Receiving the Financial Statement and Treasurer's Report for the time period ending 31 December 2003.
2.   Announcement of the Ballot Election of the Board of Directors.

By order of the Board of Directors
Leo Kemple, Secretary

ANNUAL REPORT 2003

As required in the Bylaws of the Applied Computational Electromagnetics Society, Inc. a California Nonprofit Public Benefit Corporation, this report is provided to the members. Additional information will be presented at the Annual Meeting and that same information will be included in the July Newsletter for the benefit of members who could not attend the Annual Meeting.

MEMBERSHIP REPORT

As of 31 December 2003, the paid-up membership totaled 350, with approximately 37% of those from non-U.S. countries. There were 24 full time student, unemployed and retired members; 71 industrial (organizational) members; and 255 regular members. The total membership has increased by 29% since 1 Jan 2003, with non-U.S. membership increasing by 41%.

Leo Kemple, Secretary

Validating Numerical Models - Quantifying Error [1]

Alistair Duffy   Dawn Coleby

School of Engineering and Technology,
De Montfort University, Leicester, UK
apd@dmu.ac.uk
dawn@dmu.ac.uk

Anthony Martin

MIRA Ltd, Watling Street,
Nuneaton, UK
anthony.martin@mira.co.uk

**Malcolm   Trevor Benson
Woolfson**

School of Electrical and Electronic Engineering,
Nottingham University, Nottingham, UK
Malcolm.woolfson@nottingham.ac.uk

Trevor.benson@nottingham.ac.uk

Abstract

The validation of numerical models often progresses incrementally from previous models or other numerical solutions or is undertaken by comparison with experimentally obtained reference measurements. Notwithstanding the accuracy of the reference results, quantification of the error between the two is important information in deciding the quality of the model. It is frequently the case that this estimate of error is done by eye. However, for purposes of traceability and objectivity, interest has started to focus on techniques to quantify this error in an algorithmic manner in a way that agrees with the general observations of experienced engineers. This paper reviews two of the most promising techniques, namely Feature Selective Validation (FSV) and Integrated Error against Logarithmic Frequency (IELF), putting them in the context of correlation and reliability functions.

INTRODUCTION

Validation may involve comparing the results from one numerical model with another modeling technique, another implementation using the same technique or with measurements. The issues raised here include:

- Noise, including numerical noise and implementation errors, and experimental error compound differences in the results being compared. Experience may allow those undertaking the validation to accommodate these errors. In many cases, this will not be done overtly, which causes problems in trying to capture the experience being relied upon.

- In many practical situations, for example in EMC, the results are complex. One particularly common example is the coupling to cabling where, typically this will involve cables in cavities, coaxial systems, cross-talk systems and/or multiaperture systems. These resonant structures interact producing complex looking data. The effect of this is that discrepancies in one aspect of the model can mask the accuracy of the rest of the model.

- Comparisons between models and measurements becomes entirely subjective, which increases the

communications difficulties within a team, particularly if this team is multidisciplinary (and therefore does not share similar backgrounds and experiences) or geographically separated (and hence will not develop a group tacit knowledge of such matters)

These factors are substantive arguments for the development of techniques to quantify the errors and recommended practice in using this information. This paper is concerned primarily with generating this quantitative data.

Two data sets used in this paper to represent validation data are given in Figure 1. They have been chosen because they have moderate complexity resulting from compound resonances. It is acknowledged that the actual data, to which the techniques discussed later may be applied, may have a much greater or lower feature density.
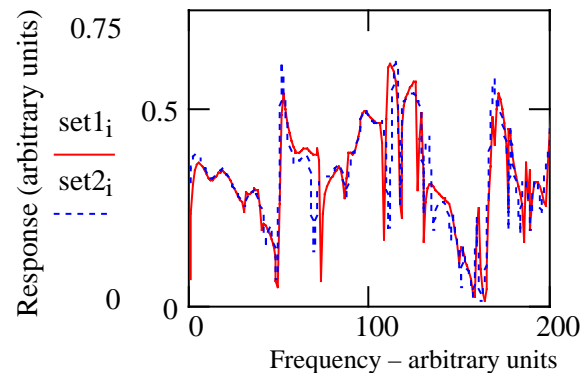
Figure 1 Two typical data sets used for comparison

It can be seen that the set of data shown in Figure 1 exhibits a very similar amplitude trend (mean level). However, there are shifted resonant-like features and some features which appear on one data set but not the other.

As noted previously, engineers typically assess the quality of such comparisons visually, with individual and group experience, both tacit and explicit, being essential in order to comment on the quality of such comparisons [1]. Those used to undertaking these comparisons often 'know' how to

---

interpret a result but can't say why: experience suggests the ambiguities and the assumptions. However, problems with human interpretation include fatigue and experiential differences between those assessing similar results, which produces different interpretations. It is also evident that these interpretations are further guided by the way in which expertise is learned, as much as the expertise at a particular instant. Thus, continuous learning may, itself, result in temporal differences, with different assessments of the same data being forthcoming at different times.

An important consideration when quantifying the differences between data sets, is that any quantitative measure should also provide a basis for investigating the quality of the comparisons. The measure should encourage the user to ask "why is that?", ideally decomposing the original comparison into something that helps in the post-mortem exercise of identifying if and how the comparison can be improved. Moreover, to aid communication, natural language descriptors should be used where possible.

The next section outlines correlation and Reliability factors, neither of which are particularly useful in this context, but worth considering as essential background: there may be circumstances in which these approaches could be beneficial. This is followed by an overview of Feature Selective Validation (FSV) and Integrated Error against Log Frequency (IELF), two techniques which have demonstrated some benefit in this application area.

CORRELATION and RELIABILITY FUNCTIONS

The *Pearson Correlation Coefficient* [2], is usually used to measure whether there is a linear relationship between two variables and the strength of the relationship. Plotting the two signals against each other on a scatter diagram is another easy method to determine the strength of the linear relationship between the compared signals, and the direction of the relationship. One study on correlation is discussed in reference [3]

To ensure that the Pearson Correlation Coefficient is accurate, several assumptions must be met. These assumptions involve the residuals of the data sets, which must be independent, normally distributed and have a constant variance. If the assumptions are not valid, log transformations of the data can be used, or an equivalent non-parametric test called *Spearman Rank Correlation* [2] can be applied. Spearman Rank Correlation measures the correlation of the ranks of the two variables. Both correlation coefficients will lie in the range –1 to +1. In most cases, the Pearson correlation coefficient is the default 'correlation'.

The Pearson Correlation Coefficient is calculated using:

$$R = \frac{\sum xy - (\sum x \sum y)/n}{\sqrt{(\sum x^2 - (\sum x)^2/n)(\sum y^2 - (\sum y)^2/n)}}$$

x=data set 1

y=data set 2

n= total number of points in both data sets

The Spearman Rank Correlation Coefficient is calculated using:

$$R = 1 - \frac{6 \times \sum (D^2)}{n(n^2 - 1)}$$

D=difference in rank of pairs x and y

The main disadvantage is that despite the general familiarity, a simple correlation does not convey much information about the richness of the data and level of discrimination in high feature density situations. It can, therefore, produce results, which do not reflect the 'by-eye' opinions [4].

A technique developed to overcome some of the limitations of correlation was the introduction of *correlelograms* [5]. These involve cross-correlating the two data sets, incrementally shifting one set against the other to determine the peak correlation and the necessary shift (a similar approach could be used for stretching operations). A symmetry measure of the cross-correlation function is then determined by taking the rms of the differences between the cross-correlelogram at point k and point f_{max} -k where k is a variable (frequency) between f_{min} and f_{max}. The final value is the difference between the auto-correlelogram (where both data sets are the reference data) and the cross-correlelogram. Figure 2 shows the cross- and auto-correlation graphs for the data sets presented in Figure 1.
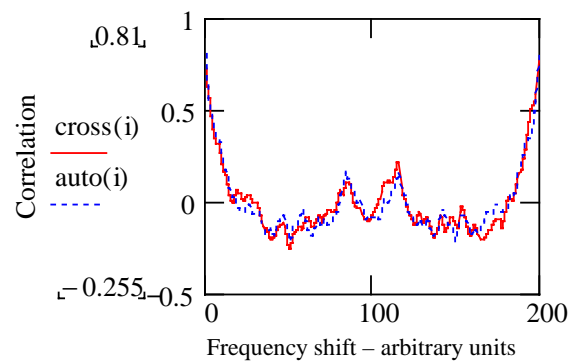

Figure 2 Correlelograms

The results are summarised in table 1

Table 1 Correlation values

Maximum correlation value	0.804
rms difference	0.051

rms symmetry	0.901

The fairly high correlation value indicates a reasonably good comparison, the difference value suggests that the results are close, reasonably uniformly across the range, and the high symmetry measure suggests that there is little skewing of the results.

One advantage of this approach is that it extends a technique which is widely accepted. The additional measures can provide a greater insight into the behavior of the system and the graphical output can assist in the overall assessment of the comparison. The disadvantage is that the additional measures have little, apparent, intuitive relevance, and relating them back to the physical systems may be difficult.

Reliability factors (R-factors) were originally used to compare transmission electron diffraction, TED, [6] and to compare calculated and measured LEED intensity spectra for surface structure determination [7]. Reliability factors were designed to analyse differences between two sets of results e.g. modelled and experimental data. Difference measures are used to compare signals and derivatives are used to compare features. Most R-factors compare the gradients, peaks and troughs of the signals being compared, albeit in different ways.

One of the R-factors considered for this work is that proposed by van Hove [8], which consists of a number of individual elements, generally comparing differences in the original data sets or differences in their derivatives, as detailed here:

$$R1 = \frac{\sum_{f\min}^{f\max} \left| I_{Set1_f} - C \cdot I_{SET2_f} \right|}{\sum_{f\min}^{f\max} \left| I_{Set1_f} \right|} \quad R2 = \frac{\sum_{f\min}^{f\max} (\left| I_{Set1_f} - C \cdot I_{SET2_f} \right|)^2}{\sum_{f\min}^{f\max} (I_{Set1_f})^2}$$

$$R3 = \frac{No.+ve\ slopes\ SET1}{No.-ve\ slopes\ SET1} - \frac{No.+ve\ slopes\ SET2}{No.-ve\ slopes\ SET2} \quad C = \frac{\sum I_{set1}}{\sum I_{set2}}$$

$$R4 = \frac{\sum_{f\min}^{f\max} \left| I'_{SET1}(f) - C \cdot I'_{SET2}(f) \right|}{\sum_{f\min}^{f\max} \left| I'_{SET1}(f) \right|} \quad R5 = \frac{\sum_{f\min}^{f\max} (I'_{SET1}(f) - C \cdot I'_{SET2}(f))^2}{\sum_{f\min}^{f\max} (I'_{SET1}(f))^2}$$

Ix represent the amplitudes of the data points in the two data sets. R1 and R2 emphasize the agreement in the locations, heights and depths of the peaks and troughs but do not concern themselves with the detail on the peaks nor the nature of curvature. R3, R4 and R5 were proposed by van Hove to overcome this. In order to provide a single figure of merit, it has been proposed [4] that a total value can be obtained from:

$$RT = \sqrt{R1^2 + R2^2 + R3^2 + R4^2 + R5^2}$$

When applied to the data of Figure 1, the van Hove method gives the results of Table 2. The low values of R1 and R2 indicate a generally good agreement. The high value of RT, derived from R4 and R5 suggest large differences in the fine-grain detail.

Table 2 Van Hove assessment of the data sets in Figure 1

R1	R2	R3	R4	R5	RT
0.136	0.052	-0.275	1.079	1.319	1.723

Modifications have been made to the van Hove method to allow the individual R factors to be derived as a function of frequency[6].

FEATURE SELECTIVE VALIDATION (FSV)[4]

The basis of the FSV technique is the decomposition of the results to be compared into only two 'component' measures and then the recombination of the results to provide a global *goodness of fit* measure. The components used are the Amplitude Difference Measure (ADM), which compares the amplitudes and 'trends' of the two data sets and the Feature Difference Measure (FDM), which compares the rapidly changing features (as a function of the independent variable). The ADM and FDM are then combined to form a global difference measure (GDM). All of the ADM, FDM and GDM are usable as point-by-point analysis tools or as a single, overall, measurement.

The ADM and FDM are obtained using the following equations.

$$ADM = \sum_{f\min}^{f\max} \frac{\left| I_{low1} - I_{low2} \right|}{\alpha_{AD1}}$$

$$FDM = 2\sum_{f\min}^{f\max} \{FD_1(f) + FD_2(f) + FD_3(f)\}$$

where

$$FD_1(f) = \frac{\left| I'_{low1} - I'_{low2} \right|}{\alpha_{FD1}}$$

$$FD_2(f) = \frac{\left| I'_{high1} - I'_{high2} \right|}{\alpha_{FD2}}$$

Also

$$FD_3(f) = \frac{\left| I''_{high1} - I''_{high2} \right|}{\alpha_{FD3}}$$

$$\alpha_{FD_1} = \frac{2}{f_{\max} - f_{\min}} \sum_{f=f_{\min}}^{f_{\max}} \left[\left| I'_{LOW1}(f) \right| + \left| I'_{LOW2}(f) \right| \right]$$

$$\alpha_{FD_2} = \frac{4}{f_{max} - f_{min}} \sum_{f=f_{min}}^{f_{max}} \left[\left| I'_{HIGH1}(f) \right| + \left| I'_{HIGH2}(f) \right| \right]$$

$$\alpha_{FD_3} = \frac{6}{f_{max} - f_{min}} \sum_{f=f_{min}}^{f_{max}} \left[\left| I''_{HIGH1}(f) \right| + \left| I''_{HIGH2}(f) \right| \right]$$

where I_{low1} and I_{low2} are the amplitude of data sets 1 and 2 at data point f. The subscript *low* refers to the low frequency components of the data sets. This is obtained by Fourier transforming the data and inverse transforming the lowest 25% of the data, i.e. the range of frequencies $0 \le f \le f_s/8$, where f_s is the sampling frequency. α_{AD1} is an amplitude normalisation factor which is the average absolute energy contained in the signals under investigation.

I_{high} is the high pass component of the data sets, obtained by Fourier Transforming the data sets and inverse transforming the highest 75%, i.e. $f_s/8 \le f \le f_s/2$. The single primes (') indicate the first derivative with respect to the x-axis of a set and the double primes (") indicate the second derivative of the data. The α denominators are normalisation factors obtained for the data set components being compared.

The Global Difference Measure (GDM) is then obtained as:

$$GDM = \sum_{f_{min}}^{f_{max}} \sqrt{(ADM(f))^2 + (FDM(f))^2}$$

The value obtained from this equation gives a single figure of merit representing the comparison of the modeled and measured data across the data points. The GDM, like the ADM and FDM, is available on a point-by-point basis. The benefit of the point-by-point results is that these can help to identify regions where attention needs to be focused during validation of the model or in the post-mortem phase.

Natural language descriptors have been assigned to the output from this technique (ideal, excellent, very good, good, fair, poor, very poor) with some success [9].

The comparison of the traces in Figure 1 yields the GDM of Figure 3, ADM of Figure 4 and FDM of Figure 5. The global figures are given in Table 3 along with their natural language descriptors.

Table 3 Overall results of the FSV comparison of the data in Figure 1

Measure	Value	Descriptor
GDM	0.3	Good
ADM	0.1	Excellent
FDM	0.3	Good
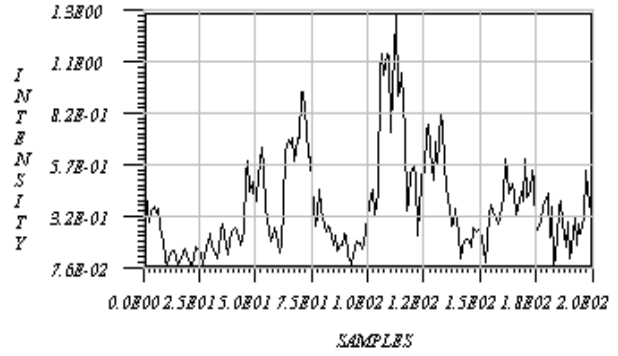
Figure 3 Global Difference Measure of the data of Figure 1
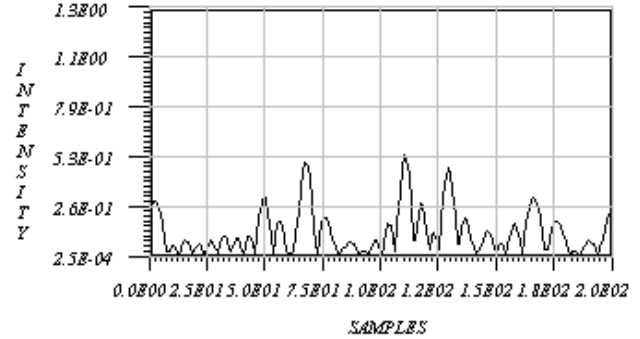
Figure 4 Amplitude Difference Measure of data in Figure 1
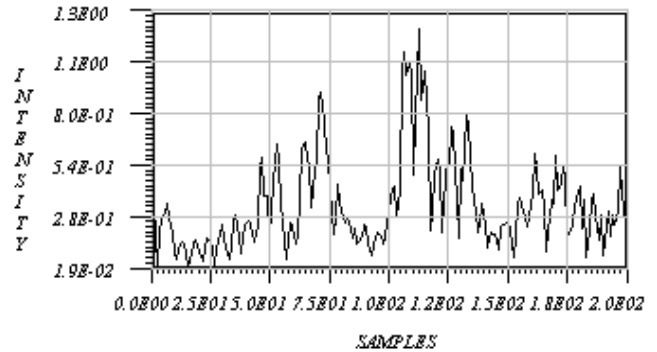
Figure 5 Frequency Difference Measure of data in Figure 1

Further, the probability density function of the individual point-by-point analyses can be plotted to provide a confidence measure. Essentially, this density function provides a visual guide as to how well a comparison conforms to the descriptor discussed above. The probability density function for the Global Difference Measure, shown in Figure 3, is given in Figure 6.
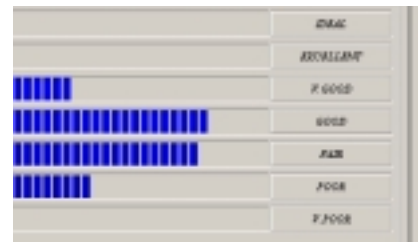
The results confirm the conclusions of a visual inspection of the source data; that is,

1. the amplitude and general trends are in excellent agreement and
2. while there are regions, which are substantially different in terms of the location of features, the overall agreement is good.

This section has demonstrated the basis of the FSV method and described how it can compare data in a tiered manner, ranging from a point-by-point analysis to a single global figure providing an overview of the whole comparison. It has the advantages of breaking down the comparison into the two main aspects generally considered, namely amplitude/trends and features, and of having a natural language description. Previous tests have shown encouraging agreement with the perceptions of practicing engineers.

INTEGRATED ERROR AGAINST LOG FREQUENCY (IELF) [8]

This technique is based on the concept that the difference between the data being compared is the most significant aspect of the comparison. Further, any comparison based on a mean value of the difference would also require the standard deviation in order to give some additional context to this figure. However, the authors' of [8] concluded that a single figure of merit could be obtained by integrating the error over the frequency range of interest. A logarithmic frequency axis was chosen. Essentially, the calculation sums the (error ×data point separation) ÷ overall range. Hence, the proposed equation for this is:

$$IELF = \frac{\sum_0^n |error_n| \cdot \{\ln(f_{n+1}) - \ln(f_{n-1})\}/2}{\ln(f_n) - \ln(f_0)}$$

- n is the number of frequencies for which there is data,
- f_0 is the first frequency, f_n is the last frequency,

and

- $error_n$ is the difference between the two sets of data for the nth frequency.

The source data in Figure 1, with the difference on a logarithmic frequency range is shown in Figure 7, w.
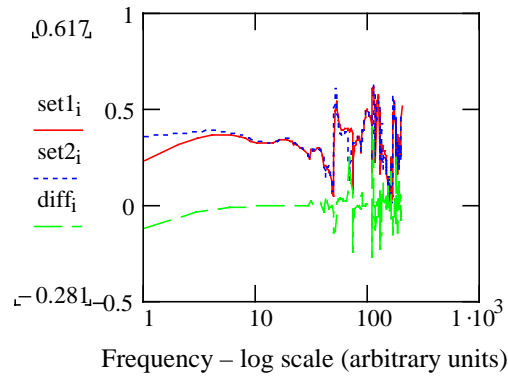
Figure 7 Original and difference data

The scaling of the IELF is such that 0 would be a perfect comparison and subsequently larger values would represent increasingly poor results. Applying the IELF to the data of Figure 1 (keeping the amplitude axis linear) gives a result of 0.9. However, this value is best used as a relative comparison with other results. Both values indicate a high level of agreement between the original data.

An advantage of this approach is that because it produces a single value which has some relevance to the way data is compared by EMC engineers, it is particularly good for ranking data resulting from many comparisons, and because the scaling axis can be readily normalized, it is easy to compare with data ranked by the engineers.

DISCUSSION

The ability to assign a numerical value between results from a numerical model and those a measurement or other models is an important factor in validating numerical models. This paper has reviewed some of the most promising candidate techniques in order to be able to do this. It should be noted that none of the techniques is limited to validation; the applications for them can extend to many other areas of engineering requiring the quantitative comparison of complex data. One of the fundamental challenges is that in order to be of practical use, any technique must provide some mirror of the way in which engineers look at the data and this implies the need to benchmark. This is a topic of current research. A method proposed to do this uses a question and answer approach to quantify comparisons [11].

REFERENCES

[1] AP Duffy, "EMC Comparison: A technical problem or a knowledge management issue?", *Zurich International EMC Symposium,* Feb 2003.
[2] See for example http://mathworld.woolfram.com
[3] Kevin J Mcdonald, *Software Tool To Compare Two Datasets*, M.Sc. Dissertation, York University, UK. April 1999.

[4] Anthony Martin, *Feature Selective Validation*, 1999 PhD Thesis, De Montfort University, Leicester.

[5] AP Duffy, M S Woolfson, T M Benson: "Use of correlation functions to assist the experimental validation of Numerical Modelling Techniques". *Microwave and Optical Technology Letters*, June 5, 1994, 7 (8), pp. 361 - 364.

[6] T. Suzuki, H. Minoda, Y. Tanishiro, K.Yagi, "TED analysis of the Si(113) surface structure."1999 *Surface Science*. Vol 438, part 1/3 pp76-82.

[7] K.Heinz, G.Besold, "Comparison of Zanazzi-Jona and Pendry reliability factors over an extended energy range.", 1983 *Journal of Physics C (Solid State Physics)*. Vol 16, pp1299-1306.

[8] Van Hove, M.A. et al (1977) "Surface structure refinement of $2H\text{-}MoS_2$, $2H\text{-}NbSe_2$ + w(100)p(2x1)-O via new reliability factors for surface crystallography", Surface Science, Vol 64, pp.85.

[9] AR Ruddle, AJM Martin, DD Ward, "Quantitative data comparisons: Applications and experiences in automotive EMC", *Zurich International EMC Symposium,* Feb 2003.

[10] RJ Simpson and CCR Jones, "IELF (Integrated Error Against Log Frequency) as a solution to quantifying comparisons" *Zurich International EMC Symposium,* Feb 2003.

[11] D Coleby and A Duffy, "The development and Validation of a New Technique to Compare Complex Data Sets", *Zurich International EMC Symposium,* Feb 2003.

Discontinuous Galerkin Methods for the Time-Domain Maxwell's Equations

An Introduction

J.S. Hesthaven[†] and T. Warburton[‡]

[†] *Division of Applied Mathematics, Brown University, Box F, Providence, RI 02912, USA*
[‡] *Department of Mathematics and Statistics, University of New Mexico, Albuquerque, NM 87131, USA*

E-mail: Jan.Hesthaven@brown.edu; timwar@unm.edu

We discuss the basic elements of the discontinuous Galerkin methods for the time-domain Maxwell's equations. A one-dimensional example is developed in detail from which the extension to two- and three-dimensional algorithms are minimal. A few examples are offered as well as guidelines for extensions, generalizations, and helpful software resources.

1. INTRODUCTION

The simplicity, robustness, and reasonable accuracy of the classical finite-difference time-domain (FDTD) method [27] for solving the time-domain Maxwell's equations has propelled this method to become the method of choice among engineers and scientist solving Maxwell's equations in the time-domain. In particular the last decade has seen an explosion in applications and developments, many driven by the very influential texts by Taflove [24, 25].

By now it is also, however, clear that the FDTD methods have severe limitations, e.g., its inherent 2nd order accuracy severely limits their ability to correctly represent wave motion over long distances unless the grid is prohibitively fine. Furthermore, the simplicity of the method, on one hand its very strength, also becomes its most severe restriction by prohibiting the accurate representation of problems in complex geometries. In recent years, a number of efforts have been aimed at addressing the shortcomings of the classical FDTD schemes, e.g., embedding schemes to overcome staircasing [5] and high-order finite difference schemes [25, 14], and body conforming nonorthogonal FDTD methods [15, 6] or contour path methods [18]. Other techniques and improvements are discussed in [24, 25]. Most of these methods, however, have not really penetrated into main stream user community, partly due to their complicated nature and partly because these methods themselves often introduce other complications.

For dealing with complex geometries, one can resort to the use of finite-volume [22]/finite element methods [17, 26], these methods are, in their classic form, 2nd

1

17

order accurate as the FDTD method. Furthermore, the finite element method becomes implicit.

For the accurate and efficient modeling of large scale EM applications the short-comings of low order methods render them impractical due to the need for fine grids to avoid prohibitive error accumulation. However, this understanding of the very source of the limitations also suggest that a high-order time-domain solution technique may offer the efficiency and accuracy required for future large scale CEM modeling capabilities. High-order methods are characterized by being able to accurately represent wave propagation over very long distances, using only a few points per wavelength and with an error accumulation rate that is significantly reduced as compared to 2nd order accurate schemes [21]. For three-dimensional large scale computations, this translates into dramatic reductions in the required computational resources, i.e., memory and execution time, and promises to offer the ability to model problems of a realistic complexity and size.

Traditionally, the development of suitable high-order solution techniques has been held back by the difficulties associated with formulating stable and high-order accurate schemes for solving wave-dominated problems in geometrically complex domains. The recent development of stable discontinuous element/Penalty methods [3] and efficient and accurate ways of representing solutions and operators on triangles and tetrahedra [9, 10, 11, 12] has paved the way for overcoming the restrictions associated with classical high-order methods. In contrast to high-order schemes based on classical finite element techniques, the approach taken here leads to fully explicit schemes.

In the following we provide a step-by-step tutorial on the key components needed to formulate and implement these methods. The methods are, by any measure, more complex that simple FDTD methods. They are not, however, as complex as one could fear, given that they offer choice of arbitrary order of accuracy and support for fully unstructured grids. Furthermore, their very formulation ensures high computational efficiency and excellent parallel performance and the generality to address related problems, e.g., frequency-domain curl-curl equations and nonlinear MHD, with only minor extensions. In the last section we shall discuss generalization and offer some pointers to software resources which should enable a short startup phase.

2.   A ONE-DIMENSIONAL DETOUR

As a way of understanding the multi-dimensional scheme for solving Maxwell's equations, let us begin by considering the central elements of the scheme for the one-dimensional Maxwell's equations

$$\varepsilon\frac{\partial E^y}{\partial t} = -\frac{\partial H^z}{\partial x} \;\; , \;\; \mu\frac{\partial H^z}{\partial t} = -\frac{\partial E^y}{\partial x} \quad x \in [0, L] = \Omega \;\; . \tag{1}$$

For simplicity we restrict the attention to a cavity type problem, with PEC boundaries, i.e., $E^y(0, t) = E^y(L, t) = 0$. Generalization to other types of boundaries, e.g, absorbing boundary conditions are straightforward.

For simplicity of the notation, we write Eq.(1) as a conservation law
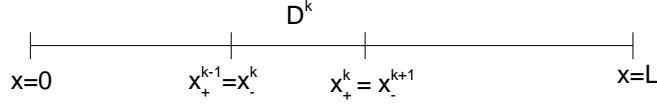
FIG. 1. Notation used in the one dimensional case.

$$\mathrm{Q}\frac{\partial \boldsymbol{q}}{\partial t} + \frac{\partial \boldsymbol{F}(\boldsymbol{q})}{\partial x} = 0 \ ,$$

where

$$\boldsymbol{q} = \left[\begin{array}{c} E^y \\ H^z \end{array} \right] \ , \quad \boldsymbol{F}(\boldsymbol{q}) = \left[\begin{array}{c} H^z \\ E^y \end{array} \right] \ , \quad \mathrm{Q} = \left[\begin{array}{cc} \varepsilon & 0 \\ 0 & \mu \end{array} \right] \ ,$$

represent the statevector of unknown fields, the flux and the materials, respectively.

We shall now assume that the domain of interest, $\Omega = [0, L]$, is segmented into K non-overlapping elements, each covering $x \in [x_-^k, x_+^k]$ and with $x_-^1 = 0$ and $x_+^K = L$, as illustrated in Fig. 1. Furthermore, we shall call the length of each element, $h^k = x_+^k - x_-^k$. With this, we construct a simple linear mapping

$$x^k(r) = x_-^k + \frac{r+1}{2} h^k \ ,$$

such that $r \in [-1, 1]$ represents a standard element of length 2.

In each of the K elements, we shall assume that the solution $\boldsymbol{q}^k(x, t) = [E^y(x^k, t), H^z(x^k, t)]^T$ can be expressed as a polynomial as

$$\boldsymbol{q}^k(x, t) = \sum_{i=0}^{N} \boldsymbol{q}^k(x_i^k, t) l_i^k(r(x)) = \sum_{i=0}^{N} \boldsymbol{q}_i^k(t) l_i^k(x^k) \ ,$$

where x_i^k represent $N+1$ grid points within the k'th element and $l_i^k(x)$ is the classical Lagrange polynomial based on these grid points, i.e.,

$$l_i^k(x) = \prod_{j=0; j \neq i}^{N} \frac{x^k - x_j^k}{x_i^k - x_j^k} \ , \quad l_i^k(x_j^k) = \delta_{ij} \ .$$

Rather than using this formula, and to maintain generality, we express the local Lagrange polynomials through the following relation

$$\boldsymbol{q}^k(x, t) = \sum_{i=0}^{N} \boldsymbol{q}_i^k(t) l_i^k(x^k) = \sum_{n=0}^{N} \hat{\boldsymbol{q}}_n^k(t) \phi_n(x^k) \ ,$$

where $\phi_n(x^k)$ is a polynomial basis defined on the interval and $\hat{q}_n^k(t)$ are the expansion or modal coefficients. While many choices are possible, e.g., a simple monomial basis, $\phi_n(x) = x^n$, for computational reasons one should use an orthonormal basis such as

$$\phi_n(x) = \frac{P_n(x)}{\sqrt{2n+1}} \quad,$$

where $P_n(x)$ represent the classical Legendre polynomial [23]. Now defining the matrix

$$\mathrm{V}_{ij} = P_j(x_i) \quad,$$

where x_j are the Legendre Gauss Lobatto quadrature points, we recover

$$\boldsymbol{q}_N^k = \mathrm{V}\hat{\boldsymbol{q}}_N^k \quad,\quad \mathrm{V}^T\boldsymbol{l}^k(x^k) = \boldsymbol{\phi}(x^k) \quad,$$

where

$$\boldsymbol{q}_N^k = \left[q_0^k, \ldots, q_N^k\right]^T \quad,\quad \hat{\boldsymbol{q}}_N^k = \left[\hat{q}^k, \ldots, \hat{q}_N^k\right]^T \quad,$$

are simply vectors of nodal and modal values and

$$\boldsymbol{l}^k(x) = [l_0^k(x^k), \ldots, l_N^k(x^k)]^T \quad,\quad \boldsymbol{\phi}(x^k) = [\phi_0(x^k), \ldots, \phi_N(x^k)]^T \quad,$$

simply represent the vector of local Lagrange polynomials and polynomial basis functions evaluated at x^k.

In this approach, the matrix V, plays a central role as the transformation between nodal values, $\boldsymbol{q}_N^k$, and modal coefficients, $\hat{\boldsymbol{q}}_N^k$, as well as a way by which to evaluate the Lagrange polynomials. In this one-dimensional case, this may seem as an unnecessarily complicated way of doing this. However, as we shall see shortly, the advantage of this approach is that it generalizes to higher dimensions and general distributions of grid points.

To arrive at the semi-discrete scheme, let us now require that local residual, i.e., the error when $\boldsymbol{q}_N^k$ is substituted into Eq.(1), vanishes in the following way

$$i \in [0, \ldots, N] \;:\; \int_{x_-^k}^{x_+^k} \left(\mathrm{Q}\frac{\partial \boldsymbol{q}_N^k}{\partial t} + \frac{\partial \boldsymbol{F}(\boldsymbol{q}_N^k)}{\partial x}\right) l_i^k(x)\, dx = 0 \quad.$$

This can be recognized as a Galerkin approach, albeit on the local element only. Integration by parts once yields

$$\int_{x_-^k}^{x_+^k} \left(\mathrm{Q}\frac{\partial \boldsymbol{q}_N^k}{\partial t}l_i^k(x) - \hat{\boldsymbol{n}}\cdot\boldsymbol{F}(\boldsymbol{q}_N^k)\frac{dl_i^k}{dx}\right)\, dx = -\oint_{x_-^k}^{x_+^k} \hat{\boldsymbol{n}}\cdot\boldsymbol{F}(\boldsymbol{q}_N^k)l_i^k(x)\, dx \quad,$$

which one can recognize as the weak Galerkin form. Here $\hat{\boldsymbol{n}}$ represent an outward pointing normal vector which, in this one-dimensional case, simply takes the values of ∓ 1 at x_-^k and x_+^k, respectively.

To complete the scheme, we must recognize that two neighboring elements will both contain the same point, e.g., $x_+^k = x_-^{k+1}$, see Fig. 1. Thus, at this point we will have two solutions and we must choose which one, or a combination of the two, is the correct. For this we shall use a numerical flux, $\boldsymbol{F}^*$,

$$\hat{\boldsymbol{n}} \cdot \boldsymbol{F}^* = \hat{\boldsymbol{n}} \cdot \boldsymbol{F}^*(\boldsymbol{q}^-, \boldsymbol{q}^+) \ ,$$

where $\boldsymbol{q}^-$ refers to the local solution and $\boldsymbol{q}^+$ the solution in the neighboring elements. There are several possible choices of this function and we return to this issue shortly. It is important to appreciate the importance of this choice as it is the numerical flux which is responsible for combining all local elementwise solution to the global solution.

With the numerical flux introduced on the right hand side to connect the elements, we do integration by parts once more to obtain the final form

$$\int_{x_-^k}^{x_+^k} \left(Q \frac{\partial \boldsymbol{q}_N^k}{\partial t} + \frac{\partial \boldsymbol{F}(\boldsymbol{q}_N^k)}{\partial x} \right) l_i^k(x)\, dx = \oint_{x_-^k}^{x_+^k} \hat{\boldsymbol{n}} \cdot \left[\boldsymbol{F}(\boldsymbol{q}^-) - \boldsymbol{F}^* \right] l_i^k(x)\, dx \ . \qquad (2)$$

To simplify matters further, assume that $Q(x)$, i.e., the material coefficients, can be taken to be constant on each element and let us define

$$M_{ij}^{1d} = \int_{x_-^k}^{x_+^k} l_i^k(x^k) l_j^k(x^k)\, dx^k = \frac{h^k}{2} \int_{-1}^{1} l_i(r) l_j(r)\, dr \ ,$$

$$S_{ij} = \int_{x_-^k}^{x_+^k} l_i^k(x^k) \frac{dl_j}{dx}\, dx^k = \int_{-1}^{1} l_i(r) \frac{dl_j}{dr}\, dr \ ,$$

as the one-dimensional mass matrix and stiffness matrix. Note in particular that due to the mapping, the matrices are the same for all elements up to a scaling constant, i.e., only one copy should be stored.

Using the transformation matrix, V, introduced above we immediately obtain

$$M^{1d} = \left(V^{-1} \right)^T V^{-1} \ , \quad S = \left(V^T \right)^{-1} W V^{-1} \ , \quad W_{ij} = \int_{-1}^{1} \phi_i(r) \phi_j'(r)\, dr \ ,$$

where the latter integrals can be computed by quadrature or by using properties of the orthogonal polynomials.

Before writing down the final scheme, let us discuss choices of the numerical flux, $\boldsymbol{F}^*$. As this flux is responsible for combining the local solutions into a global solution, these choices are clearly important.

One natural condition is that the resulting scheme must be consistent, i.e, the exact solution must satisfy the scheme when refining the grid. A simple central flux would ensure this, i.e.,

$$\hat{\boldsymbol{n}} \cdot \boldsymbol{F}^*(\boldsymbol{q}^-, \boldsymbol{q}^+) = \frac{1}{2} \left[\boldsymbol{F}(\boldsymbol{q}^+) + \boldsymbol{F}(\boldsymbol{q}^-) \right] \ .$$

The advantage of this choice is its simplicity and energy conservation. However, for general (multidimensional) problems an upwind flux is superior. To derive this numerical flux one takes advantage of the fact that Maxwell's equations propagates waves around and, at any point, one can always determine which way information is propagating by considering characteristic variables. This yields

$$
\hat{\boldsymbol{n}} \cdot \boldsymbol{F}^* = \frac{1}{2} \left\{ \begin{array}{l} \overline{Z}^{-1} \left(\hat{n}_x \left\{ Z H^z \right\} + [\![E^y]\!] \right) \\ \overline{Y}^{-1} \left(\hat{n}_x \left\{ Y E^y \right\} + [\![H^z]\!] \right) \end{array} \right. , \tag{3}
$$

where $[\![q]\!] = q^- - q^+$ represent the local jump in function value and $\{ q \} = q^+ + q^-$. The material parameters of the problem are given by

$$
Z^\pm = \sqrt{\frac{\mu^\pm}{\varepsilon^\pm}} \ , \ \ Y^\pm = \left(Z^\pm \right)^{-1} \ ,
$$

represent the local impedance and conductance with the average values

$$
\overline{Z} = \frac{Z^+ + Z^-}{2} \ , \ \ \overline{Y} = \frac{Y^+ + Y^-}{2} \ .
$$

Combining Eq.(2) with the upwind flux, Eq.(3), and the definition of the matrix operators above yields the local semi-discrete scheme

$$
\begin{aligned}
\varepsilon^k \frac{h^k}{2} \mathrm{M}^{1d} \frac{d \boldsymbol{E}_N^k}{dt} + \boldsymbol{S} \boldsymbol{H}_N^k = \ & \boldsymbol{e}_0 \left[\frac{1}{\overline{Z}} \left(-Z^+ [\![\boldsymbol{H}_N^k]\!] - [\![\boldsymbol{E}_N^k]\!] \right) \right]_{x_-^k} \\
+ \ & \boldsymbol{e}_N \left[\frac{1}{\overline{Z}} \left(Z^+ [\![\boldsymbol{H}_N^k]\!] - [\![\boldsymbol{E}_N^k]\!] \right) \right]_{x_+^k} ,
\end{aligned} \tag{4}
$$

$$
\begin{aligned}
\mu^k \frac{h^k}{2} \mathrm{M}^{1d} \frac{d \boldsymbol{H}_N^k}{dt} + \boldsymbol{S} \boldsymbol{E}_N^k = \ & \boldsymbol{e}_0 \left[\frac{1}{\overline{Y}} \left(-Y^+ [\![\boldsymbol{E}_N^k]\!] - [\![\boldsymbol{H}_N^k]\!] \right) \right]_{x_-^k} \\
+ \ & \boldsymbol{e}_N \left[\frac{1}{\overline{Y}} \left(Y^+ [\![\boldsymbol{E}_N^k]\!] - [\![\boldsymbol{H}_N^k]\!] \right) \right]_{x_+^k} .
\end{aligned} \tag{5}
$$

Here $(\boldsymbol{E}_N^k, \boldsymbol{H}_N^k)$ are the vectors of locally unknown fields on element k and $\boldsymbol{e}_i$ is a N+1 long i'th unit vector. Also $[\ \cdot \ ]_a$ refers to evaluation of what is inside the bracket at $x = a$.

Since M^{1d} is entirely local, it can be inverted initially, making the semi-discrete scheme fully explicit. Furthermore, the discontinuous nature of the formulation is trivially parallel, essential to address large scale problems. We also note that all operations can be cast as simple matrix-vector (or in the case of many elements, matrix-matrix) operations which are both straightforward to implement and offers high performance.

Equations (4)-(5) represents the basic scheme at all interior element interfaces. At the metallic outer boundaries, one simply defines

$$E_+^0 = -E_-^1 \quad , \quad H_+^0 = H_-^1 \quad ,$$

and likewise at the right end, i.e., one is imposing the Dirichlet conditions by a simple mirror principle.

Without going into details, one can prove the following error estimate for the above scheme [11]

$$\|\boldsymbol{q}(t) - \boldsymbol{q}_N(t)\| \leq \frac{h^\sigma}{N^s}\|\boldsymbol{q}(0) - \boldsymbol{q}_N(0)\|_s + t\frac{h^{\sigma-1}}{N^{s-2}}\max_{t\in[0,T]}\|\boldsymbol{q}(t)\|_s \quad . \tag{6}$$

Here $\|\cdot\|$ is the global energy norm, $\|\cdot\|_s$ is the energy norm of the first s-derivatives (the Sobolev norm), and $\sigma = \max(s, N+1)$, while h is maximum element length, h^k.

Thus if the solution, $\boldsymbol{q}$, is smooth, i.e., $\|q\|_s$ is bounded for high values of s, we have hp-convergence. Furthermore, the error can grow at most linearly in time and the growth rate decays rapidly with increasing order.

This highlights the advantages of this method with general order elements, N, of general length h and with a very slow error accumulation of time, making it ideally suited for long time integration problems.

The semi-discrete scheme, Eqs.(4)-(5), can be written schematically as

$$\frac{d\boldsymbol{q}_N}{dt} = \boldsymbol{G}(\boldsymbol{q}_N, t) \quad ,$$

i.e., it is simply a system of ordinary differential equations. These can be solved using a variety of different methods, with a popular choice being a standard 4th order explicit Runge-Kutta scheme

$$\begin{aligned}
\boldsymbol{K}_1 &= \boldsymbol{G}(\boldsymbol{q}_N(t), t) \\
\boldsymbol{K}_2 &= \boldsymbol{G}(\boldsymbol{q}_N(t) + 0.5\Delta t\boldsymbol{K}_1, t + 0.5\Delta t) \\
\boldsymbol{K}_3 &= \boldsymbol{G}(\boldsymbol{q}_N(t) + 0.5\Delta t\boldsymbol{K}_2, t + 0.5\Delta t) \\
\boldsymbol{K}_4 &= \boldsymbol{G}(\boldsymbol{q}_N(t) + \Delta t\boldsymbol{K}_3, t + \Delta t) \\
\boldsymbol{q}_N(t + \Delta t) &= \boldsymbol{q}_N(t) + \frac{\Delta t}{6}\left(\boldsymbol{K}_1 + 2\boldsymbol{K}_2 + 2\boldsymbol{K}_3 + \boldsymbol{K}_4\right) \quad .
\end{aligned}$$

A rigorous expression for the stable time step, Δt, is not known, but good estimate is

$$\Delta t \leq \text{CFL}\min_\Omega \sqrt{\varepsilon^k\mu^k}\Delta x^k = \text{CFL}\min_\Omega \sqrt{\varepsilon^k\mu^k}h^k\Delta r \quad ,$$

with CFL being of $\mathcal{O}(1)$ and $min\Delta r \simeq CN^{-2}$.

To illustrate the performance of the above scheme, let us consider the simple test case of a metallic cavity, $x \in [-1, 1]$, filled with two different nonmagnetic materials. The material interface is assumed to be at $x = 0$ and the two materials have $\varepsilon_r = 1.0$ and $\varepsilon_r = 2.25$ respectively. The exact solution is well known [5].
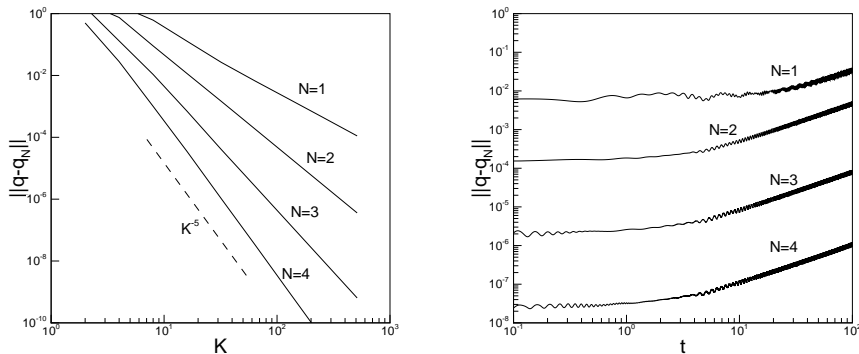
FIG. 2.   On the left is shown the global error at final time $T = 1$ for the one-dimensional cavity problem solved using K elements, each with N'th order polynomials. On the right is shown the time-dependence of the error with $K = 64$ elements, confirming linear growth.

In Fig. 2 we illustrate the accuracy of the computed solution at $T = 1$, confirming the essence of the error estimate given in Eq.(6, i.e., both h ($= K^{-1}$, decreasing the grid size) and p (increasing the local polynomial order) convergence is achieved. In Fig. 2 we also illustrate the very limited accumulation of errors over time, in accordance with the above result.

This all suggests that these methods are well suited for situations where

• High-accuracy and large dynamic range in solution is required

• Long time integration is needed

• Electrically large problems, requiring minimal points per wavelength to achieve a reasonable accuracy.

These are clearly all properties of relevance to problems of the future and, more pressing perhaps, for many current technology problems.

Furthermore, as we shall discuss in the following, the approach outlined for the very simple one-dimensional problem generalizes with minimal changes to problems requiring three-dimensional fully unstructured grids and very complex, realistic geometries.

3.   EXTENSION TO TWO DIMENSIONS

With the detailed derivation of the one-dimensional scheme above, the extension to two- (or three-) dimensional problems is relatively straight forward. In the following we shall highlight the general approach to see the similarities and minor differences.

For simplicity, we consider the two-dimensional form of Maxwell's equations, e.g.,

$$\varepsilon \frac{\partial E^x}{\partial t} = \frac{\partial H^z}{\partial y} \ , \tag{7}$$

$$\varepsilon \frac{\partial E^y}{\partial t} = -\frac{\partial H^z}{\partial x} \ ,$$

$$\mu \frac{\partial H^z}{\partial t} = \frac{\partial E^x}{\partial y} - \frac{\partial E^y}{\partial x} \ ,$$

known as the TE form. The dual form is found simply by substituting (E^x, E^y, H^z) with $(H^x, H^y, -E^z)$ and exchange ε and μ. This yields the TM form.

In both cases we have

$$\hat{\boldsymbol{n}} \times [\![\boldsymbol{E}]\!] = \hat{\boldsymbol{n}} \times [\![\boldsymbol{H}]\!] = 0 \ ,$$

i.e., tangential continuity, at all nonmetallic interfaces. At a PEC boundary

$$\hat{\boldsymbol{n}} \times \boldsymbol{E} = \hat{\boldsymbol{n}} \cdot \boldsymbol{H} = 0 \ .$$

In both cases, $\hat{\boldsymbol{n}}$ represents an outward pointing normal vector.

3.1.   The Nodal Element

The key difference between the one-dimensional and the multidimensional scheme is that the latter has to allow for the modeling of problems in geometrically complex settings, i.e., it does not suffice to consider simple dimension-by-dimension extensions of the one-dimensional approach.

To ensure this geometric flexibility, we assume that the computation domain, Ω, can be filled by some standard element, D^k, e.g., triangles or quadrilaterals. We shall furthermore assume that this multi-element grid is performed in a geometry and material conforming way, i.e., elements are assumed to have edges aligned with material/metallic interfaces.

Following the one-dimensional approach, it is clear that with the local element, D^k, we should seek an orthogonal polynomial basis, $\phi_i(\boldsymbol{x})$, as well as a set of grid points, $\boldsymbol{x}_i^k \in \mathsf{D}^k$. For the quadrilateral, one could simply use a dimension-by-dimension extension of the one-dimensional case. Let us therefore focus on the case of triangles which also has the main interest due to its geometric flexibility, possibility of utilizing existing finite element/finite volume grid generation software, and ease of exploring adaptive strategies.

The number of grid points needed per triangle is

$$N = \frac{(n+1)(n+2)}{2} \ ,$$

which also becomes the number of local unknowns. Here n is the order of the local polynomial approximation. The question we must address is where to put these grid points, e.g., there is no obvious extension of the one-dimensional case.

As for the one dimensional case we shall assume the existence of a mapping which maps the standard right angle triangle, $\mathsf{I} : \{(r,s) \in [-1,1]; r+s \leq 0\}$, to
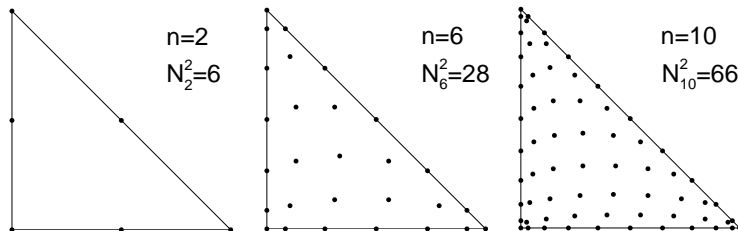
FIG. 3.   Examples of nodal distributions in the triangle for different orders, n, of approximation. N_n^2 lists the total number of grid points.

the particular triangle, D^k. Assuming for simplicity that D^k is straightsided, this mapping is simply given as

$$\boldsymbol{x}^k(r,s) = -\frac{r+s}{2}\boldsymbol{v}_1^k + \frac{1+r}{2}\boldsymbol{v}_2^k + \frac{1+s}{2}\boldsymbol{v}_3^k \ , \tag{8}$$

where $\boldsymbol{v}_i^k$ represent the 3 vertices of D^k and $(r,s) \in \mathsf{I}$ are the coordinates in the standard triangle while $\boldsymbol{x}^k \in \mathsf{D}^k$. From this simple map, we can compute the metric of the mapping, needed for computing derivatives as we shall see shortly, as well as the transformation Jacobian. An important observation to make is that the transformation Jacobian, J, is a constant for any straightsided triangle, D^k. The details are all given in [9, 10] and is essentially a generalization of the one-dimensional case.

The choice of the nodal distributions inside the triangle has received some attention recently and such distributions, allowing for the construction of well behaved unique Lagrange polynomials up to order 19, can be found in [8]. There are exactly N grid points in a triangle and, furthermore, the nodes along the edges are the one dimensional Legendre Gauss Lobatto points, also used in Sec. 2. A few examples of how the grid point distributions look like are shown in Fig. 3.

An orthonormal basis on the triangle is given as [20]

$$\tilde{\psi}_i(\boldsymbol{r}) = P_{\alpha_1}^{(0,0)}\left(\frac{2(r+1)}{(1-s)}-1\right)\left(\frac{1-s}{2}\right)^{\alpha_1} P_{\alpha_2}^{(2\alpha_1+1,0)}(s) \ ,$$

$$i = \alpha_1 + n\alpha_2 - \frac{\alpha_2}{2}(-1+\alpha_2) + 1 \ ,$$

$$\gamma_i = \left(\frac{2}{2\alpha_1+1}\right)\left(\frac{1}{\alpha_1+\alpha_2+1}\right) \ ,$$

$$\psi_i(\boldsymbol{r}) = \frac{\tilde{\psi}_i(\boldsymbol{r})}{\sqrt{\gamma_i}} \ . \tag{9}$$

$P_n^{(\alpha,\beta)}(x)$ represents the classical Jacobi polynomial of order n [23], e.g., $P_n^{(0,0)}(x)$ is the Legendre polynomial also used in the one dimensional case.

This may seem a bit complicated. However, there are standard ways of computing/evaluating Jacobi polynomials and software for doing so can be found from online sources (see Sec. 5).

With this, all essential operators, i.e., mass and stiffness matrices as well as the transformation matrix V, can be defined and generated exactly as in the one-dimensional case discussed in the above.

3.2. The Scheme

With the local elementwise treatment in place, we can continue the development of the global scheme. As in the one dimensional case, we write, for simplicity, Maxwell's equations as

$$Q\frac{\partial \boldsymbol{q}}{\partial t} + \nabla \cdot \boldsymbol{F}(\boldsymbol{q}) = 0 \ ,$$

where Q represent the materials, $\boldsymbol{q}$ the 3-vector of fields and $\boldsymbol{F}(\boldsymbol{q})$ the flux. The detailed definition of these depends on which polarization is considered, i.e., for the TE form we have

$$Q = \begin{bmatrix} \varepsilon & 0 & 0 \\ 0 & \varepsilon & 0 \\ 0 & 0 & \mu \end{bmatrix} \ , \quad \boldsymbol{q} = \begin{bmatrix} E^x \\ E^y \\ H^z \end{bmatrix} \ , \quad \boldsymbol{F}(\boldsymbol{q}) = \begin{bmatrix} 0 & -H^z \\ H^z & 0 \\ E^y & -E^x \end{bmatrix} \ .$$

Exactly as in the one dimensional case we shall require that the polynomial approximation

$$\boldsymbol{q}_N^k(\boldsymbol{x}, t) = \sum_{i=1}^N \boldsymbol{q}^k(\boldsymbol{x}_i^k, t) L_i^k(\boldsymbol{x}^k) \ ,$$

satisfies the equation as

$$\forall k \ : \ \int_{\mathsf{D}^k} \left(Q\frac{\partial \boldsymbol{q}_N^k}{\partial t} + \nabla \cdot \boldsymbol{F}_N^k \right) L_i^k(\boldsymbol{x}^k) \, d\boldsymbol{x}^k = \oint_{\partial \mathsf{D}^k} L_i^k(\boldsymbol{x}^k)\hat{\boldsymbol{n}} \cdot \left[\boldsymbol{F}_N^k - \boldsymbol{F}^* \right] \, d\boldsymbol{x}^k \ . \tag{10}$$

Specifying the numerical flux, $\hat{\boldsymbol{n}} \cdot \boldsymbol{F}^*$, follows exactly the same lines as in the one-dimensional case, i.e., a central flux is obtained directly from the average of the two fluxes while the upwind flux can be derived from the general three-dimensional expression

$$\hat{\boldsymbol{n}} \cdot [\boldsymbol{F} - \boldsymbol{F}^*] = \begin{cases} \overline{Z}^{-1} \boldsymbol{n} \times (-Z^+ [\![\boldsymbol{H}]\!] + \boldsymbol{n} \times [\![\boldsymbol{E}]\!]) \\ \overline{Y}^{-1} \boldsymbol{n} \times (Y^+ [\![\boldsymbol{E}]\!] + \boldsymbol{n} \times [\![\boldsymbol{H}]\!]) \end{cases} \ . \tag{11}$$

This suffices to write down the local two-dimensional scheme for TE scheme as

$$\varepsilon^k J^k M^{2d} \frac{\partial \boldsymbol{E}_N^x}{\partial t} - S_y \boldsymbol{H}_N^z = F\left[\frac{\hat{n}_y}{\overline{Z}} \left(-Z^+ [\![\boldsymbol{H}_N^z]\!] + [\![\boldsymbol{E}_T]\!] \right) \right] \ , \tag{12}$$

$$\varepsilon^k J^k M^{2d} \frac{\partial \boldsymbol{E}_N^y}{\partial t} + S_x \boldsymbol{H}_N^z = F\left[\frac{\hat{n}_x}{\overline{Z}} \left(Z^+ [\![\boldsymbol{H}_N^z]\!] - [\![\boldsymbol{E}_T]\!] \right) \right] \ ,$$

$$\mu^k J^k \mathrm{M}^{2d} \frac{\partial \boldsymbol{H}_N^z}{\partial t} - \mathrm{S}_y \boldsymbol{E}_N^x + \mathrm{S}_x \boldsymbol{E}_N^y = \mathrm{F}\left[\frac{1}{\overline{\overline{Y}}}\left(Y^+ \llbracket \boldsymbol{E}_T \rrbracket + \llbracket \boldsymbol{H}_N^z \rrbracket\right)\right] \quad.$$

Here $(\boldsymbol{E}_N^x, \boldsymbol{E}_N^y, \boldsymbol{H}_N^z)$ represent the N-long vectors of unknowns on the element D^k and we have defined $\boldsymbol{E}_T = \hat{\boldsymbol{n}} \times \boldsymbol{E}$ as the tangential component of $\boldsymbol{E}$ along the boundary of the element. Furthermore, (ε^k, μ^k) represent the local material parameters and J^k represents the local transformation Jacobian, recovered from Eq.(8).

Most of what remains in the above translates exactly from the one-dimensional case, e.g., M^{2d} represents the local mass matrix constructed directly from V; the stiffness matrices S_x and S_y are given as

$$\mathrm{M}^{2d} = \left(\mathrm{V}^{-1}\right)^T \mathrm{V}^{-1} \quad.$$

$$\mathrm{S}_r = \left(\mathrm{V}^T\right)^{-1} \mathrm{W}^r \mathrm{V}^{-1} \quad, \quad \mathrm{W}_{ij}^r = \int_{\mathsf{D}^k} \phi_i(\boldsymbol{r}) \frac{\partial \phi_j(\boldsymbol{r})}{\partial dr} d\boldsymbol{r} \quad,$$

$$\mathrm{S}_s = \left(\mathrm{V}^T\right)^{-1} \mathrm{W}^s \mathrm{V}^{-1} \quad, \quad \mathrm{W}_{ij}^s = \int_{\mathsf{D}^k} \phi_i(\boldsymbol{r}) \frac{\partial \phi_j(\boldsymbol{r})}{\partial ds} d\boldsymbol{r} \quad,$$

where $\boldsymbol{r} = (r, s)$ are the local coordinates in the reference element. Using the chain rule this simply yields

$$\mathrm{S}_x = S_r \frac{\partial r}{\partial x} + S_s \frac{\partial s}{\partial x} \quad, \quad \mathrm{S}_y = S_r \frac{\partial r}{\partial y} + S_s \frac{\partial s}{\partial y} \quad,$$

where the matrix coefficients are obtained directly from the mapping given in Eq.(8).

The main difference between Eqs.(4)-(5) and Eq.(12) is found in the matrix F which is the finite dimensional approximation of the surface integral.

$$\oint_{\partial \mathsf{D}^k} L_i^k(\boldsymbol{x}^k) \hat{\boldsymbol{n}} \cdot \left[\boldsymbol{F}_N^k - \boldsymbol{F}^*\right] d\boldsymbol{x}^k = \oint_{\partial \mathsf{D}^k} L_i^k(\boldsymbol{x}^k) g(\boldsymbol{x}) \, d\boldsymbol{x} \quad,$$

where $g(\boldsymbol{x})$ has been introduced for simplicity. This clearly breaks into 3 edge integrals ($l = 1, 2, 3$) of the form

$$\oint_{\partial \mathsf{D}_l^k} L_i^k(\boldsymbol{x}^k) g(\boldsymbol{x}) \, d\boldsymbol{x} = \oint_{\partial \mathsf{D}_l^k} l_i^k(\boldsymbol{x}^k) \sum_{j=0}^n g(\boldsymbol{x}_j) l_j^k(\boldsymbol{x}^k) \, d\boldsymbol{x} \quad,$$

where $l_i^k(x)$ is the one-dimensional Lagrange polynomial based on the grid points along the edge l, i.e.,

$$\mathrm{M}_{ij}^{1d} = \oint_{\partial \mathsf{D}_l^k} l_i^k(\boldsymbol{r}^k) l_j^k(\boldsymbol{r}^k) \, d\boldsymbol{r} \quad,$$

is simply the one-dimensional mass matrix. Note that the two-dimensional Lagrange polynomial, $L_i^k(\boldsymbol{x}^k)$, restricted to the one-dimensional edge reduces the familiar one-dimensional Lagrange polynomial, $l_i^k(\boldsymbol{x}^k)$, due to uniqueness of the polynomials. If we now define the R_l is an $(n+1) \times N$ restriction operator that
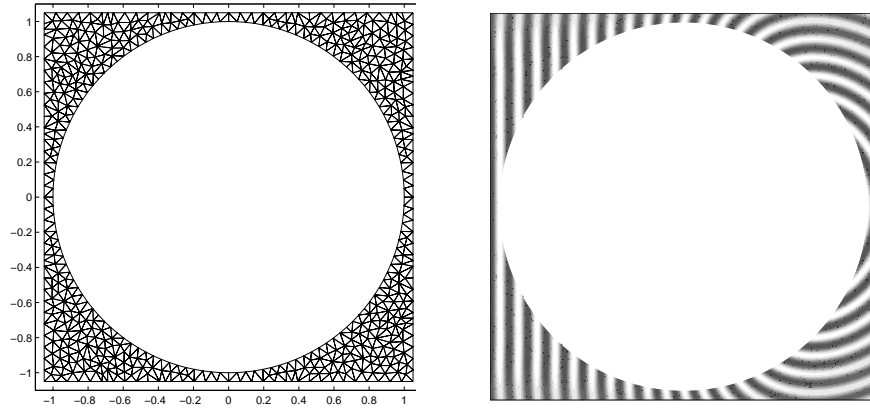
FIG. 4. On the left is shown finite element grid (950 elements) used to model plane wave TM scattering of a $ka = 20\pi$ metallic cylinder. A snapshot of E^z is shown on the right. The computational domain is terminated with high-order global boundary conditions.

extracts the $(n+1)$ nodes along edge l, then the edge integral along edge l is given as

$$\oint_{\partial \mathsf{D}_l^k} L_i^k(\boldsymbol{x}^k) g(\boldsymbol{x}) \, d\boldsymbol{x} = s_l \mathrm{R}_l^T \mathrm{M}^{1d} \mathrm{R}_l \boldsymbol{g} \quad ,$$

where s_l is the Jacobian associated with mapping the edge length to the standard interval $[-1, 1]$. The complete operator edge operator then becomes

$$\mathrm{F} = \sum_l s_l \mathrm{R}_l^T \mathrm{M}^{1d} \mathrm{R}_l \quad .$$

Clearly the components of this can be computed a priori for the standard element added with the geometry weights.

The semi-discrete form of the equations, Eq. 12, can be advanced in time using the 4th order Runge-Kutta discussed in the above with a time-step scaling like

$$\Delta t \leq \mathrm{CFL} \min_\Omega \sqrt{\varepsilon^k \mu^k} \frac{h}{n^2} \quad ,$$

where h is the smallest edge length of the element.

3.3. A Few Examples

In the following we shall offer a few examples of two- and three-dimensional tests. The emphasis here is on evaluation and verification of the scheme. Many other examples, including hard benchmarks and very large scale application, can be found in [11, 12, 14].

As a first, and familiar example, we consider plane wave TM scattering of a $ka = 20\pi$ metallic cylinder. As simple as the case is, it allows for a thorough
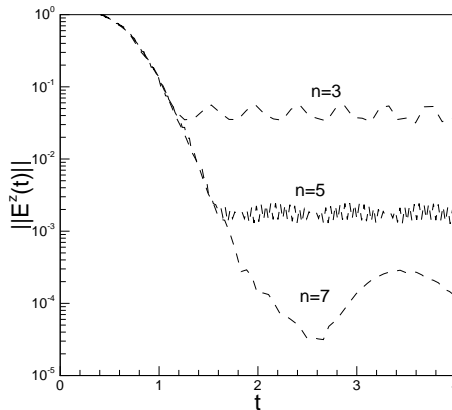
FIG. 5.   The error in E^z for plane wave TM scattering by a $ka = 20\pi$ metallic cylinder as a function of time for increasing resolution.

validation through the exact solution. We use 950 elements and an high-order local boundary condition [7]. The grid as well as a snapshot of E^z is shown in Fig. 4.

To measure the accuracy of the solution we compute the error in E^z as a function of time for increasing resolution. The results are shown in Fig. 5. For 5th order polynomials $n = 5$ there are 8-10 points per wavelength. The results confirm exponential convergence as expected. This is also a indication of the excellent performance of the high order local boundary conditions which is introduces errors well below the approximation error.

As a slight more challenging, although still two-dimensional, test case we consider plane wave TM scattering by a 'Pacman' shaped metallic cylinder. The grid, containing approximately 3800 elements, and a snapshot the E^z component is shown in Fig. 6. To truncate computational domain we use in this case a perfectly matched layer [25], to illustrate that one can terminate the domain in a variety of ways as appropriate.

This scattering problem does not have a known exact solution. To estimate the accuracy of the computed result we consider the convergence of the bistatic radar cross section (RCS). In Fig. 7 we show the computed RCS obtained using 3 different orders of approximation, clearly suggesting convergence. This example not only illustrates the ability to solve general problems but also highlights the added flexibility one has by using a high order methods on a general grid. Without having to redo the computational grid, a time consuming process for general geometries, one can obtain a sequence of solutions of increasing accuracy by simply raising the local order of approximation. This dual path to a converged result is one of the significant advantages of a flexible hp-type scheme as it decreases the significant complications associated with grid generation. Furthermore, high order elements are found to be significantly more robust to elements with bad aspect ratio.

As a final example, we consider the computation of eigenfrequencies of a $[-1, 1]^3$ PEC air filled cube. The computation is done by initially having a broadband pulse which excite a number resonant frequencies. By doing a Fourier transform of a time
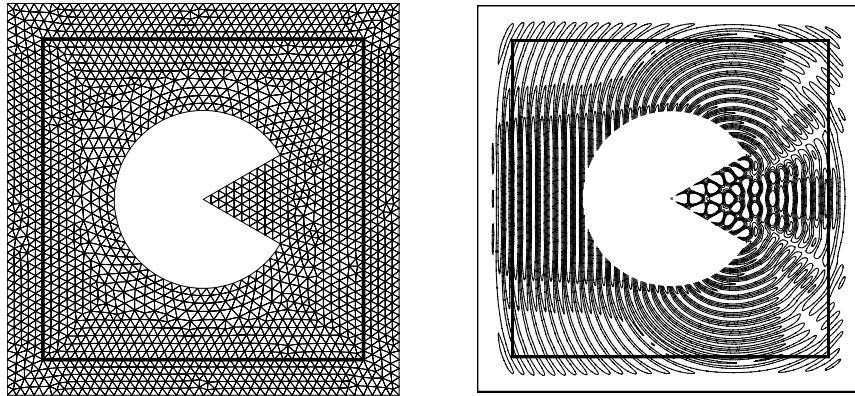
FIG. 6.   On the left is shown finite element grid (3800 elements) used to model plane wave TM scattering of a Pacman shaped metallic cylinder. A snapshot of E^z is shown on the right. A Perfectly Matched Layer (PML) is used to terminate the computational domain.

trace one can then compute the resolved modes. In this simple case, the resonant frequencies are given as

$$\omega = \pi\sqrt{m^2 + n^2 + l^2}; m + n + l \geq 2 \ \ .$$

We solve the problem by tiling the cube with 286 tetrahedra, each of 4th order, and advance the initial conditions for 250 fundamental periods. The results are shown in Fig. 8.

The results in Fig. 8 not only confirms that the correct eigenfrequencies are reproduced but also suggests that at least frequencies of $\omega \simeq 20$ is well resolved. This correspond to wave numbers between 6 and 7. With about $K^{1/3} \simeq 6.5$ element per edge and 5 grids points per edge, this corresponds to 4-5 points per wavelength, clearly demonstrating the excellent performance of a high order method even while using a coarse grid.

4. FURTHER EXTENSIONS AND GENERALIZATIONS

The most natural extension of the schemes discussion above is to include full three-dimensional Maxwell's equations. As we have seen in the last example of the previous section this is certainly possible. In fact, going from two- to three-dimensions introduces nothing new from the two-dimensional case discussed in detail in the last section. Once the nodes [9] and the orthogonal polynomials are identified, all the operators can defined and the scheme formulated. The three-dimensional flux is already given in Eq. (11). The only new component is that the F matrix now must correspond to a surface and not a line integral. The details of how to do this as well as numerous examples, further details of implementation, full analysis, and examples of parallel performance are discussed in [11, 12].
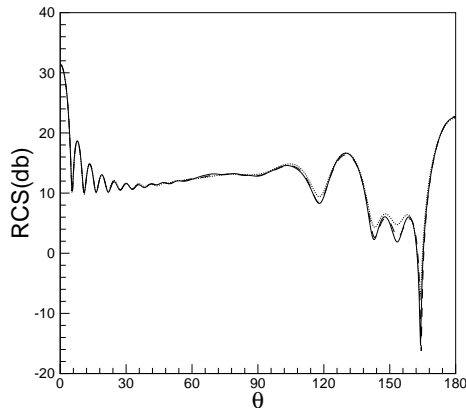
FIG. 7.   Bistatic RCS(db) computed for Pacman shaped metallic cylinder in Fig. 6. Computation done using 3rd, 5th, and 7th order approximations and results plotted on same scale, confirming convergence.

The discontinuous Galerkin formulation does not, in contrast to FDTD methods, preserve the divergence free nature of the fields, although the associated error is well controlled and generally negligible. Some efforts have focused on this issue, either by having additional slaved variables which are approximations to divergence free fields [12], or by using a locally divergence free basis [4]. In both cases only local divergence is preserved.

Another relevant issues is that of time stepping, something we dealt with in the above by using a simple 4th order Runge-Kutta method. However, the local nature of the formulation enables the elegant use of local time stepping as discussed in [2]. Other important extensions to deal with locally refined grids are explicit-implicit methods [1] as well as low storage methods [19].

With the significant success of the above methods for solving the time-domain Maxwell's equations, one can speculate whether the same formulation can be used to solve the curl-curl equation of harmonic problems or even eigenvalue problems. Questions of this character has been considered in [13, 16], concluding that this is indeed possible and paves the way for a completely general discontinuous Galerkin approach for solving Maxwell's equations both in frequency and time-domain.

5.   CONCLUSIONS AND FURTHER INFORMATION

It has been the intention of this little manuscript to offer an introduction to the formulation and development of discontinuous Galerkin methods for solving the time-domain Maxwell's equations. As we have seen, these methods have matured to a level where their implementation is relatively straightforward and resulting in algorithms which are flexible, efficient, accurate, and robust.

Many further examples and validations can be found in the listed references. Furthermore, at HTTP://WWW.USEME.ORG numerous other examples and animations are displayed. This page also contains examples and extensions of the same essential formulation to enable solution of magnetohydrodynamics and gasdynamics.
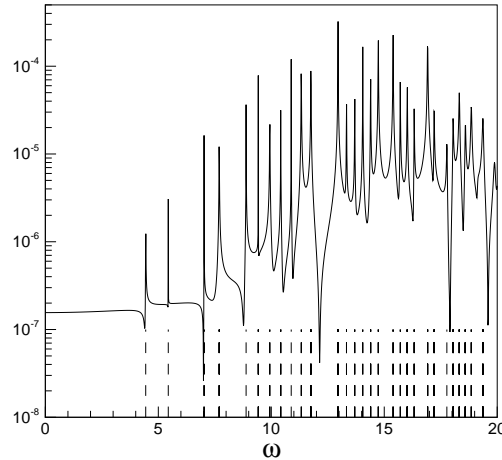
FIG. 8. Eigenfrequencies in a $[-1, 1]^3$ PEC cavity, computed by the Fourier transform of a time series of 500 periods. 286 4th order fully unstructured tetrahedral grid was used. The solid line represents the computed spectrum while the vertical dashed lines signify the exact solution, $\omega = \pi\sqrt{m^2 + n^2 + l^2}; m + n + l \geq 2$.

A small startup company, HyPerComp Inc. (HTTP://WWW.HYPERCOMP.NET) is pursuing the development of a commercial environment based on these techniques.

However, as we all know and appreciate, doing is superior to anything else when it comes to understanding a new idea. For this purpose we implemented both one and two-dimensional versions of the algorithms in Matlab and will make these scripts available to interested parties. The key elements in these implementations are a set of files, one for each order, which contains the nodal coordinates in the standard element, the critical V matrix, the one- and two-dimensional mass matrices, M^{1d} and M^{2d}, the restriction matrix, R, as well as the stiffness matrix, S. This suffices to completely specify the local scheme and should enable a very short startup time in the development and exploration of these methods as it more or less reduces the solution problem to one of grid generation and logistics.

The scripts and files as well as further information can be downloaded from HTTP://WWW.DAM.BROWN.EDU/USEME or by contacting the authors.

ACKNOWLEDGMENT

REFERENCES

1. M. H. Carpenter and C. A. Kennedy, *Fourth order 2N-storage Runge-Kutta scheme*, NASA-TM-109112, NASA Langley Research Center, VA. 1994.

2. C. Chauviere, J. S. Hesthaven, A. Kanevsky, and T. Warburton, *High-Order Localized Time Integration for Grid-Induced Stiffness.* 2nd MIT Conference on Fluid Dynamics, Boston, 2003. Vol II, 1883-1886.

3. B. Cockburn and C.W. Shu, *Runge-Kutta Discontinuous Galerkin Methods for Convection-Dominated Problems*, J. Sci. Comput. **16**(2001), pp. 173-261.

4. B. Cockburn, F. Li, and C.W. Shu, *Locally Divergence Free Discontinuous Galerkin Methods for the Maxwell Equations*, J. Comput. Phys. **194**(2004), pp. 588-610.

5. A. Ditkowski, K. Dridi, and J. S. Hesthaven, *Convergent Cartesian Grid Methods for Maxwell's Equations in Complex Geometries*, J. Comput. Phys. **170**(2001), pp. 39-80.

6. M. Fusco, *FDTD Algorithm in Curvilinear Coordinates*, IEEE Trans. Antennas Propaga. **38**(1990), pp. 76-89.

7. T. Hagstrom and T. Warburton, *A New Auxiliary Variable Formulation of High- Order Local Radiation Boundary Conditions: Corner Compatibility Conditions and Extensions to First Order Systems*, Wave Motion, 2004 – to appear.

8. J. S. Hesthaven, *From Electrostatics to Almost Optimal Nodal Sets for Polynomial Interpolation in a Simplex*, SIAM J. Numer. Anal. **35**(1998), pp. 655-676.

9. J. S. Hesthaven and D. Gottlieb, *Stable Spectral Methods for Conservation Laws on Triangles with Unstructured Grids*, Comput. Methods Appl. Mech. Engin. **175**(1999), pp. 361-381.

10. J. S. Hesthaven and C. H. Teng, *Stable Spectral Methods on Tetrahedral Elements*, SIAM J. Sci. Comput. **21**(2000), pp. 2352-2380.

11. J. S. Hesthaven and T. Warburton, *High-Order Nodal Methods on Unstructured Grids. I. Time-Domain Solution of Maxwell's Equations*, J. Comput. Phys. **181**(2002), pp. 1-34.

12. J. S. Hesthaven and T. Warburton, *High-Order Accurate Methods for Time-domain Electromagnetics*, Comput. Model. Engin. Sci. 2003 – to appear.

13. J. S. Hesthaven and T. Warburton, *High Order Nodal Discontinuous Galerkin Methods for the Maxwell Eigenvalue Problem*, Phil. Trans Royal Soc. London A, 2004 – to appear.

14. J. S. Hesthaven, *High-Order Accurate Methods in Time-Domain Computational Electromagnetics: A Review*, Adv. Imaging Elec. Phys. **127**, pp. 59-123.

15. R. Holland, *Finite Difference Solutions of Maxwells Equations in Generalized Nonorthogonal Coordinates*, IEEE Trans. Nuclear Sci. **30**(1983), pp. 4589-4591.

16. P. Houston, I. Perugia, A. Schneebeli, and D. Schötzau, *Interior Penalty Method for the Indefinite Time-Harmonic Maxwell Equations*, SIAM J. Numer. Anal. 2004 – to appear.

17. J. M. Jin, *The Finite Element Method in Electromagnetics.* John Wiley & Sons, Inc. 1993.

18. T.G. Jurgens, A. Taflove, K. Umashaankar, and T.G. Moore, *Finite-Difference Time-Domain Modeling of Curved Surfaces*, IEEE Trans. Antennas Propaga. **40**(1992), pp. 357-366.

19. C. A. Kennedy and M. H. Carpenter, *Additive Runge-Kutta Schemes for Convection-Diffusion-Reaction Equations*, Appl. Numer. Math. **44**(2003), pp. 139-181.

20. T. Koornwinder, *Two-variable Analogues of the Classical Orthogonal Polynomials* in "Theory and Application of Special Functions", R.A. Askey ed., Academic Press, 1975. pp. 435-495.

21. H. O. Kreiss and J. Oliger, *Comparison of Accurate Methods for the Integration of Hyperbolic Problems*, Tellus **24**(1972), pp. 199-215.

22. A. H. Mohammadian, V. Shankar, and W. F. Hall, *Computation of Electromagnetic Scattering and Radiation using a Time-Domain Finite-Volume Discretization Procedure*, Comput. Phys. Comm. **68**(1991), pp. 175-196.

23. G. Szegö, *Orthogonal Polynomials.* Colloquium Publications **23**, American Mathematical Society, Providence, RI. 1939.

24. A. Taflove, *Computational Electrodynamics. The Finite-Difference Time-Domain Method.* Artech House, Boston, 1995.

25. A. Taflove (Ed.), *Advances in Computational Electrodynamics: The Finite-Difference Time-Domain Method*, Aztech House, Boston, 1998.

26. J.L. Volakis, A. Chatterjee and L. Kempel, *Finite Element Methods for Electromagnetics: Antennas, Microwave Circuits and Scattering Applications.* IEEE Press, 1998.

27. K. S. Yee, *Numerical Solution of Initial Boundary Value Problems involving Maxwells Equations in Isotropic Media*, IEEE Trans. Antennas Propaga. **14**(1966), pp. 302-307.

WIDEBAND PLANAR SLOT ANTENNAS

Abdelnasser A. Eldek, Atef Z. Elsherbeni, Charles E. Smith and Kai-Fong Lee

Center of Applied Electromagnetic Systems Research (CAESR)
Department of Electrical Engineering, The University of Mississippi, University, MS 38677

Abstract — **In this paper a printed dipole antenna and three slot antennas are designed to operate at 10 GHz for use in radar systems. A parametric study of each antenna and comparison between their radiation properties including return loss, bandwidth, directivity, efficiency and radiation patterns for 6-element linear array are introduced. Slot antennas show wider bandwidth, less coupling and smaller antenna size compared with the microstrip printed dipole.**

I. INTRODUCTION

In present-day radar systems, the need for antennas of small size and high efficiency has generated much attention in the study of compact microstrip antennas. These antennas exhibit low profile and lightweight properties as well as low cross polarization radiation in some designs. However, microstrip antennas inherently have narrow bandwidths (BW) and in general are half-wavelength structures operating at the fundamental resonant mode [1]. The coplanar patch antennas (CPAs) introduced in [2] and [3] have 3.4% and 8.8% BW, respectively. Researchers have made efforts to overcome the problem of narrow BW and various configurations have been presented to extend the BW. Adding a short on the upper slot of the CPA and varying its length achieved 30 to 40% BW [4] at higher frequencies for radar applications. A number of bow-tie slot designs are recently introduced, which demonstrate wide bandwidth that ranges from 17% to 40% [5-10].

In this paper, printed dipole, coplanar patch-slot (CPA), slot dipole and bow-tie slot antennas have been designed for radar applications with emphasis on size reduction, and improved BW, coupling and efficiency for antenna arrays. Characteristics of arrays of 6 elements of these antennas are compared with the printed dipole design, and their S-parameters and radiation properties are introduced.

II. ANTENNA ANALYSIS

The numerical analysis of the antennas studied is performed using the commercial computer software package, Momentum of Agilent Technologies, Advanced Design System (ADS), which is based on the method of moment (MoM) technique for layered media. Momentum solves mixed potential integral equations (MPIE) using full wave Green's functions. First, a comparison of the results of ADS with measured results of a CPA presented in [2] reveals good agreement, as shown in Fig. 1, and this gives credibility to the results of the ADS simulation. Another verification for the results of ADS is confirmed by a comparison with the results from a simulation based on the finite difference time domain (FDTD) technique.

A. *Printed Dipole Antenna*

The geometry of a printed dipole and its parameters are shown in Fig. 2, where *W* represents the dipole width, L_f is the feed line length, *t1* is the dipole height, *t2* is the feed line width and *G* is the gap width. In addition to these parameters, *h* is the height of the substrate, and ε_r is the dielectric constant.
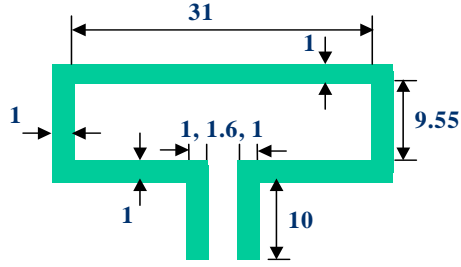
Substrate with backed ground plane, where
$\varepsilon_r = 2.17$ and h = 0.508 (height).
All dimensions are in mm.
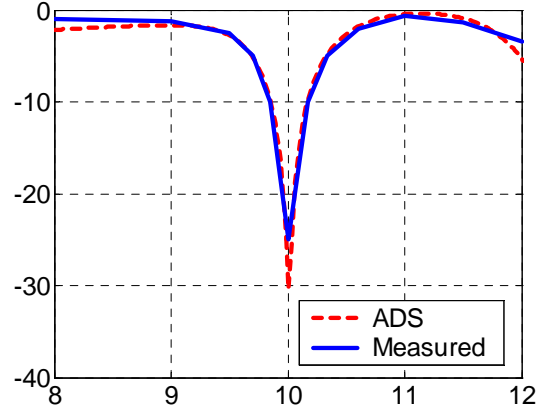
Fig. 1. Verification with measured results of the CPA presented in [2].

The return loss of the printed dipole based on ADS Momentum is confirmed by comparing the numerical results from a FDTD computation. This comparison reveals good agreement, as shown in Fig. 3. The presented printed dipole has (W, $t1$, $t2$, G, l_f and h) = (12.4, 0.5, 0.3, 0.4, 0.3 and 1.57 mm) and ($\varepsilon_r = 2.2$).

The parametric study of this structure starts with the feed line length L_f. By increasing L_f, it is noticed that the resonant frequency decreases, then increases back towards the original frequency at certain length. It is known that the input impedance for a transmission line is given by

$$Z_{in} = Z_0 \frac{Z_L + jZ_0 \tan \beta l}{Z_0 + jZ_L \tan \beta l}.$$

$$(1)$$

At $l = \lambda g/2$, $Z_{in} = Z_L$, and, from this, a numerical experiment can be performed to define λg of this antenna. Then, the effective permittivity, ε_{reff}, can be calculated from

Fig. 2. Printed dipole antenna parameters.

Fig. 3. ADS Momentum and FDTD results for the printed dipole antenna.

$$\lambda_g = \frac{\lambda_0}{\sqrt{\varepsilon_{reff}}} \ . \tag{2}$$

The λg of this printed dipole is 23 mm and ε_{reff} is about 1.7, which is 77% of ε_r. LineCalc, a program within the ADS software package, calculates ε_{reff} of the two strip feed line to be 1.78 which shows that the printed dipo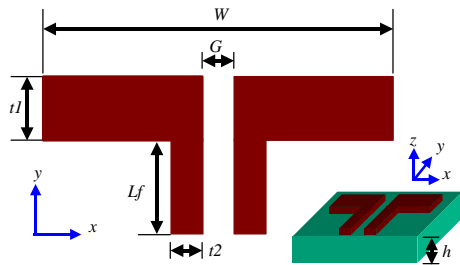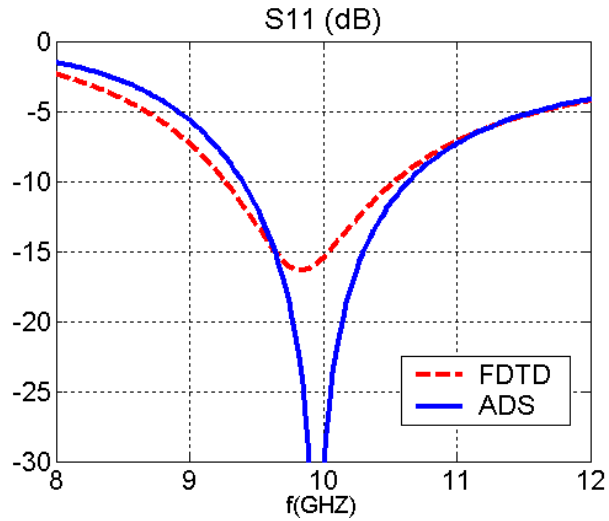le antenna structure decreases the feed line $\varepsilon_{reff.}$ Additional parametric study for this antenna shows that increasing W, h and ε_r reduces the resonant frequency, and that $t1$ and the feed line parameters control the return loss level. Further study shows that the dominant factor in the design of printed dipoles is W, which traditionally assumed to be $\lambda_g/2$. This antenna has more than 12 % BW and 90 % efficiency.

B. Slot Dipole Antenna

The slot dipole geometry and its parameters are shown in Fig. 4, where W represents the dipole width, $S1$ is the slot height, L_{cpw} is the length of the coplanar waveguide (CPW) feed line, and $S2$ and G are the width and gap width of the CPW. In addition to these parameters, h is the height of the substrate, and ε_r is the dielectric constant.

The slot dipole presented in this paper has for the following parameters, W, $S1$, L_{cpw}, $S2$, G and h, the values 19.3, 1.5, 1.5, 0.25, 1, and 1.57 mm and $\varepsilon_r =2.2$. Figure 5 shows a comparison between ADS Momentum and FDTD results for the presented slot dipole. This comparison reveals good agreement and confirms our design procedure using Momentum.

$Lcpw$ behaves like L_f in the printed dipole, and λ_g and ε_{reff} are calculated by the same procedure used previously. The calculated λ_g of the slot dipole is found to be 23.5 mm and $\varepsilon_{reff} = 1.63$ (74% of ε_r), respectively. The ε_{reff} of the CPW feed line based on LineCalc calculations is 1.576, which shows that the slot dipole antenna structure increases the feed line $\varepsilon_{reff.}$ By observing the influence of various parameters on the antenna performance, it is found that increasing W, $S1$, h and ε_r decreases the resonant frequency, and $S1$ and the feed line parameters control the return loss level. Further study shows that the total slot length, calculated at the centerline of the slot, is about λ_g and W is about 0.82 λ_g. This antenna can provide more that 21 % BW and 80 % efficiency.
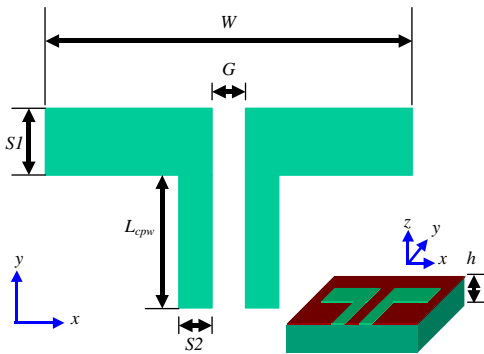

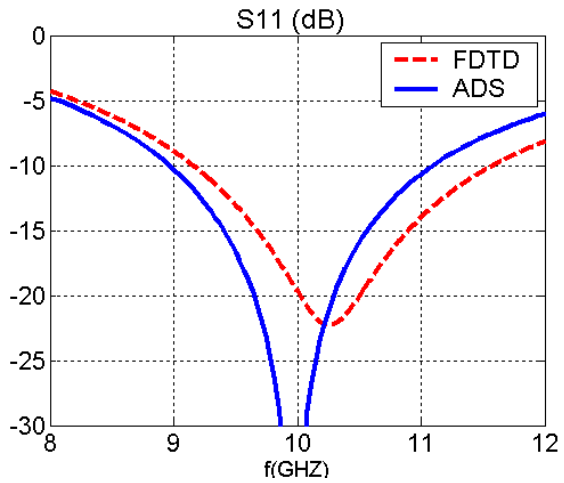Fig. 4. Slot dipole geometry and parameters.

Fig. 5. ADS Momentum and FDTD results for the slot dipole antenna.

C. Coplanar Patch-Slot Antenna

The geometry of the CPA and its parameters are shown in Fig. 6. The antenna consists of a rectangular patch surrounded by a non-uniform width slot. As shown in Fig. 6, *W* represents the patch width, *L* is the patch length, and *S1*, *S2* and *S3* are the widths of the upper slot, left-right slot, and lower slot, respectively. *S4* and *S5* are the gap width and feed line width of the CPW, and *Lcpw* represents the length of the CPW. In addition to these parameters, *h* is the height of the substrate, and ε_r is the dielectric constant.

The dimensions of the CPA presented in this paper and the antenna of [2] are shown in Table 1. The presented CPA does not have conductor-backed ground plane while the CPA of [2] has one. A comparison between these two antennas shows an improvement in BW from 3.4 % to 17 %, as shown in Fig. 7. Furthermore, the presented CPA is 60 % less in width than that of [3]. Figure 8 shows a comparison between ADS and FDTD results for the presented CPA. This comparison reveals good agreement.

For this antenna, *Lcpw* also behaves like L_f in the printed dipole antenna design, and λ_g and ε_{reff} are calculated, using the same procedure used for the dipole, to be 23.5mm and 1.54 (70 % ε_r), respectively. LineCalc calculation of ε_{reff} of the CPW feed line is 1.58, which shows that the CPA antenna decreases the feed line ε_{reff}. By observing the influence of various parameters on the antenna performance, it is found that increasing *W*, *L*, *h*, ε_r, *S1* and *S2* and decreasing S3 reduce the resonant frequency. The CPW feed line parameters control the return loss level. Although the effect of all these parameters is clear on f_c, it is not clear which one parameter can primarily increase the BW of the antenna. In CPA design, the dominant factors are *W*, *L* and the total slot length (*Ltotal*), calculated at the centerline of the slot, where

$$Ltotal = 2(W+L+Lcpw+S2+S3)+S1-S4-S5. \tag{3}$$

By studying the given design at various center frequencies, it is clear that *W* is about $0.5\lambda_g$, and the *Ltotal* is about $1.5\lambda_g$. At the same time *L* is about $0.1\lambda_g$. In general, *Ltotal* controls the resonant frequency while patch dimensions and slot widths control the level of return loss and the resulting BW. Our study revealed that this antenna yields more that 17 % BW and 80 % efficiency.
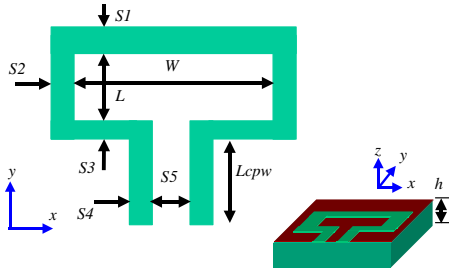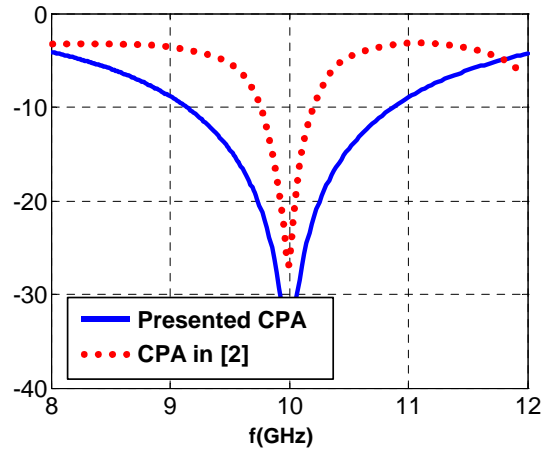

Fig. 6. CPA geometry and parameters.

Fig. 7. Return loss comparison between the presented CPA and that of [3].

Table 1. Dimensions in mm of the CPA of [2] and the presented CPA antenna working at 10 GHz.

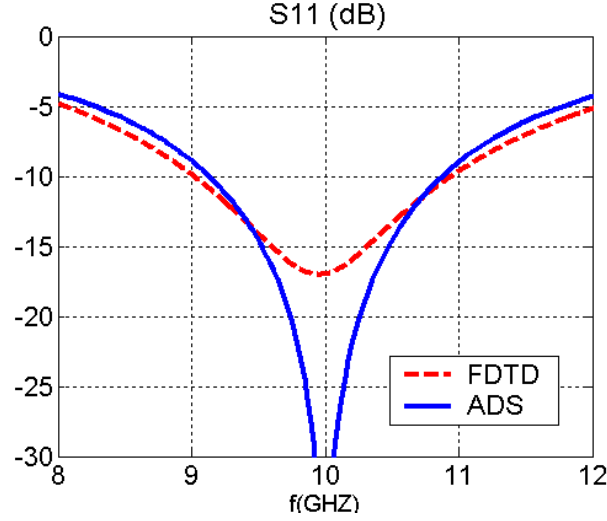|	W	L	L_{cpw}	$S1:S5$	h	ε_r
CPA of [2]	31	9.55	10	1, 1, 1, 1, 1.6	0.508	2.17
Presented CPA	12.4	2.0	1.5	0.5, 0.25, 0.5, 0.25, 0.75	1.57	2.2

Fig. 8. Comparison between the ADS Momentum and FDTD results for the presented CPA.

D. Bow-Tie Slot Antenna

The geometry of the bow-tie slot antenna and its parameters are shown in Fig. 9, where W_1 represents the width, L_{cpw} is the feed line length, L_1, L_2, L_3, L_4 and W_2 define the bow shape, and S_1 and S_2 define the feed line parameters. In addition to these parameters, h is the height of the substrate, and ε_r is the dielectric constant. The presented bow-tie design has the parameters W_1, W_2, L_1, L_2, L_3, L_4, L_{cpw}, S_1, S_2, and h being set equal to 22.9, 8.7, 3.5, 20.75, 19.45, 7.35, 18.5, 0.25, 3, and 1.57 mm, respectively, and $\varepsilon_r=2.2$. Figure 10 shows a comparison between ADS Momentum and FDTD results for the presented bow-tie slot antenna. Although a stair case geometry is used in FDTD approach to define the bow-tie geometry, and only one cell is used in the feed line slot due to memory restrictions, the comparison reveals acceptable agreement, which confirms our design procedure using Momentum.

It is found that $Lcpw$ behaves similar to L_f as in the printed dipole, and λ_g, and ε_{reff} are calculated to be 22.5 mm and 1.78 (80 % ε_r), respectively, using the same procedure. LineCalc calculates ε_{reff} of the bow-tie slot feed line to be 1.51, which shows that the bow-tie clearly increases the feed line $\varepsilon_{reff.}$ By observing the influence of various parameters on the antenna performance, it is found that resonant frequency decreases when increasing h, ε_r, W, $L2$ and $L4$, and, when decreasing $W2$, $L1$, $L3$ and $S1$ and increasing $S1$, $L1$ and $L3$, increases the BW. It is also determined that the feed line dimensions control the return loss level at the center frequency. By studying the given design at various center frequencies, it is clear that W is about λ_g and the $L4$ is about $0.3\lambda_g$. This antenna can yield more than 40 % BW and 80 % efficiency.

The bow-tie slot antenna is fabricated and the return loss is measured using the HP 8510C vector network analyzer (VNA). The fabricated antenna has a finite ground plane truncated at 1 cm away from the bow-tie slot edge. Figure 11 shows the antenna and the coaxial connector used to feed it. The antenna with finite ground plane is simulated using ADS Momentum and Fig. 12 presents the measured and simulated results, which reveals a good agreement. The measured return loss for the finite ground plane bow-tie slot antenna has a bandwidth of 52%, which is better than the simulation results.
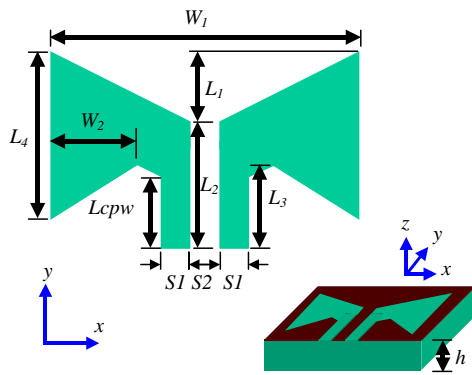

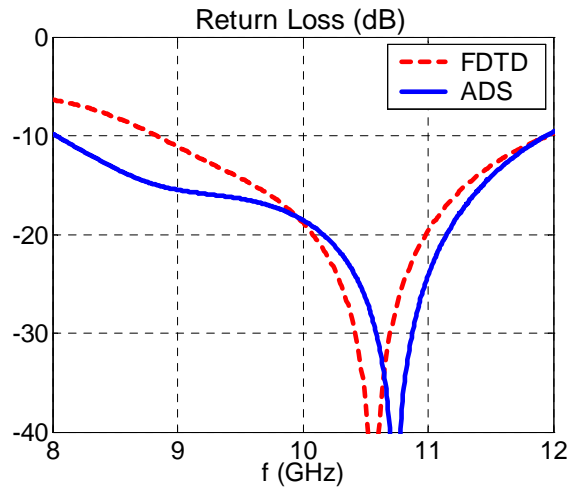Fig. 9. Bow-tie slot antenna geometry. and parameters.

Fig. 10. Comparison between the ADS Momentum and FDTD results for the presented Bow-tie slot antenna.
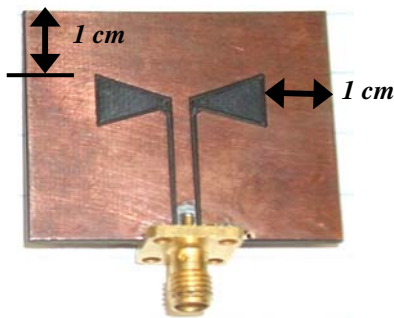

Fig. 11. The finite ground plane bow-tie slot antenna used in measurement.
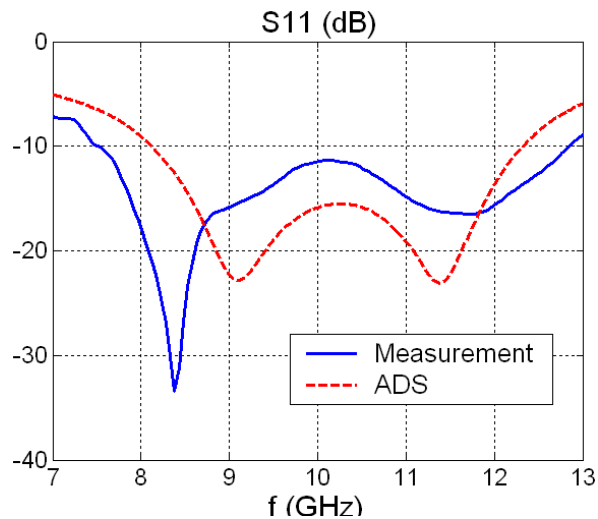
Fig. 12. Measured and ADS Momentum results of the finite ground plane bow-tie slot antenna.

III. SINGLE ELEMENT CHARACTERISTICS

Figures 3, 5, 8 and 10 show that the *BW* of the printed dipole antenna, the CPA, the slot dipole and the bow-tie are 12.5 %, 17 %, 21 % and 40 %, respectively. The stability of the radiation properties of each antenna, as a single element, in the operating band has been investigated. Table 2 shows the stability characteristic of each antenna by showing directivity (*D*), gain (G) and efficiency (η) at selected frequencies covering the entire operating band. In general, all the antennas show good stability over the entire band. The radiation patterns of the presented antennas are shown in Figures 13, 14 and 15 in *x-y*, *x*-z and *y*-z plane, respectively. The printed dipole has no radiation in *x*-y plane, while the slot antennas radiate in *x*-y as shown in Fig. 13. In the *x*-z plane, the cross polarization level of the printed dipole antenna is less than -40 dB, the slot dipole -32 dB, the bow-tie -27 dB and the CPA -17 dB. In the *y-z* plane, the cross polarization level is 40 dB, which is why E_θ is not shown for the printed dipole and E_ϕ is not shown for the slot antennas. Antenna polarization and its relation with the radiation pattern are discussed in the next section for each antenna.

Table 2. Properties of the 4 presented antennas (single element) at selected frequencies covering the entire band.

Printed dipole			
Freq. (GHz)	*D (dB)*	*G (dB)*	*%η*
9.40	3.05	2.03	79.07
9.80	3.12	1.99	77.09
10.2	3.19	1.96	75.34
10.6	3.27	1.92	73.28
Slot Dipole			
Freq. (GHz)	*D (dB)*	*G (dB)*	*%η*
9.00	3.11	2.20	81.10
9.70	3.34	2.36	79.80
10.5	3.58	2.55	78.89
11.2	3.85	2.78	78.16
CPA			
Freq. (GHz)	*D (dB)*	*G (dB)*	*%η*
9.10	2.84	2.00	82.41
9.70	2.93	2.03	81.28
10.3	3.02	2.07	80.35
10.9	3.10	2.10	79.43
Bow-Tie			
Freq. (GHz)	*D (dB)*	*G (dB)*	*%η*
8.00	3.01	2.38	86.50
9.00	3.61	2.86	84.14
10.67	4.27	3.40	81.85
12.00	4.94	4.06	81.66

Fig. 13. Radiation pattern for single element in x-y plane.

Fig. 14. Radiation pattern for single element in x-z.
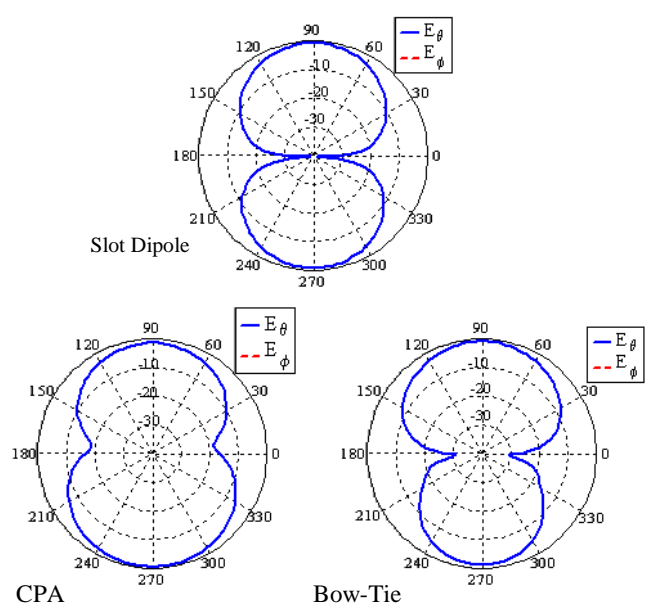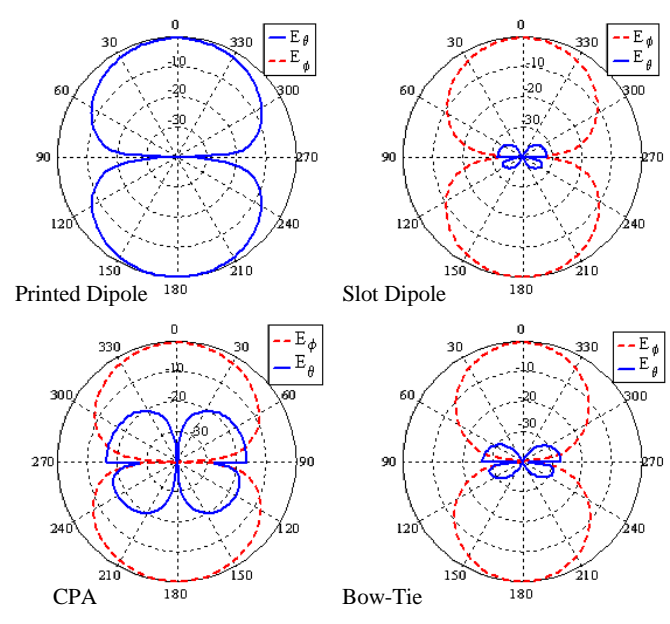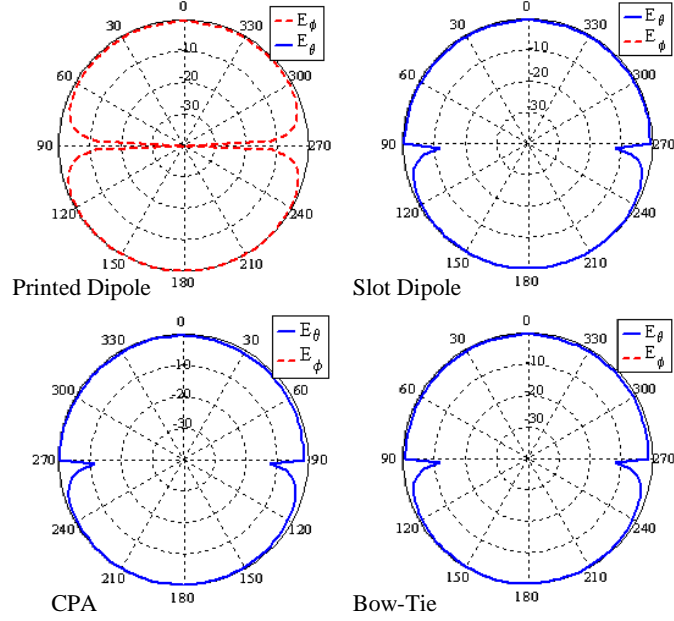
Fig. 15. Radiation pattern for single element in y-z planes.

A. Printed Dipole Antenna

The printed dipole is *x*-polarized because the electric current flows in *x*-direction as shown in Fig. 16. According to the antenna polarization and boundary conditions, the well known dipole-type radiation pattern can be expected. In the *x*-*y* plane, E_θ is normal to the direction of the polarization therefore it is zero. However E_ϕ is in the direction of the polarization at $\phi = \pi/2$, thereby it has a maximum there, but this maximum is less that 40 dB for this antenna. In the *x*-*z* plane, E_θ is in the direction of polarization at $\theta = \pi/2$, therefore it has a maximum at this angle, and it is zero at $\theta = 0$ because it is normal to the polarization direction, as shown in Fig. 14. At the same plane, *x*-z, E_ϕ is normal to the direction of polarization, therefore it is zero, as shown in Fig. 14. In the *y*-*z* plane, E_θ is normal to the direction of polarization, therefore it is also zero as shown in Fig. 15. At the same plane, *y*-z, E_ϕ is always in the direction of polarization, thus it should be uniform in this plane; however, because E_ϕ is tangential to the conductor at $\theta = \pi/2$, it goes to zero there, as shown in Fig. 15.

B. Slot Antennas

The slot antennas are *y*-polarized because, as shown in Figures 17, 18 and 19, the electrical fields tend to add in the *y*-direction and cancel each other in *x*-direction. According to the related antenna polarization and boundary conditions, a complimentary slot-dipole type radiation pattern is obtained. In the *x*-*y* plane, E_θ is normal to the conductor, but because the antennas are *y*-polarized, E_θ has a maximum only in the *y*-direction, as shown in Fig. 13. In the *x*-y plane, E_ϕ must be zero because it is tangential to the conductor, as shown in Fig. 13. In the *x*-*z* plane, E_θ is normal to antenna polarization; therefore, it is expected to go to zero. But because E_θ is normal to the conductor at $\theta = \pi/2$, it has its maximum value there; however, this maximum is affected by the surface waves on the conductor and the dielectric, as shown in Fig. 14, where E_θ is zero at $\theta = 0$, and it has a maximum at $\theta = \pi/2$. This E_θ maximum in the *x*-z plane is larger for the CPA and smaller in the slot dipole. At the same plane, *x*-z, E_ϕ is in the direction of polarization, therefore it is

the co-polarized component, and, at $\theta = \pi/2$, it is zero because it is tangential to the conductor, as shown in Fig. 14. In the *y-z* plane, E_θ is in the direction of polarization at $\theta = 0$ and normal to the conductor at $\theta = \pi/2$; therefore, it has a uniform amplitude in this plane, but this uniformity is affected by the surface waves on the conductor and the dielectric at $\theta = \pi/2$, as shown in Fig. 15. At the same *y-z* plane, E_ϕ is always normal to the polarization direction and therefore it goes to zero, and that is shown in Fig. 15.
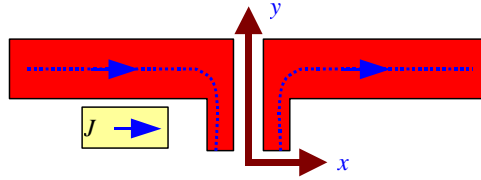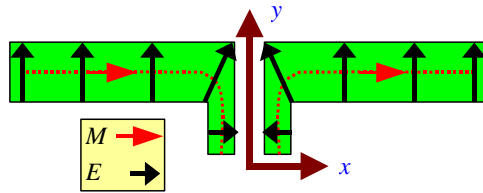

Fig. 16. Polarization in printed dipole.
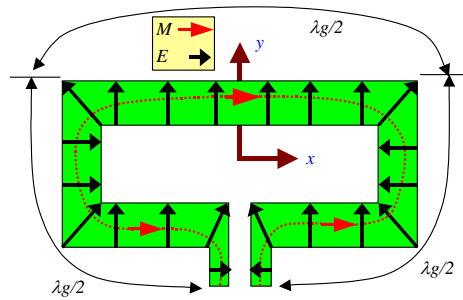

Fig. 17. Polarization in slot dipole.
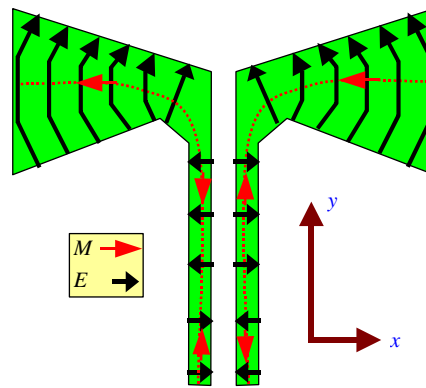

Fig. 18. Polarization in CPA.

Fig. 19. Polarization in bow-tie slot antenna.

IV. ANTENNA ARRAY CHARACTERISTICS

A. Return Loss and Coupling

Arrays of the presented microstrip slot antennas, the slot dipole, the CPA and the bow-tie slot, along with the printed dipole antenna are designed. A comparison between 6-element array modules of these antennas is performed for operation at 10 GHz. For the 6-elemnt array module, the distance between elements is chosen to provide a –24 dB magnitude for S21 (coupling between two neighboring elements). This distance is found to be 20.8 mm for the printed dipole, 4 mm for the slot dipole, 8.5 mm for the CPA and 4 mm for the bow-tie slot antenna, which indicates that the slot dipole and the bow-tie have the lower coupling and the printed dipole has the highest coupling for the same distance between elements. The return loss and coupling between elements for all designs are shown in Fig. 20. The bow-tie has 40 % *BW*, the slot dipole 21.5 %, and the CPA 17 %. The bow-tie has the lowest coupling levels between the first element and the other five elements; and the slot dipole and the CPA have the next lowest couplings.

B. Radiation Properties

Table 3 lists the BW, *D*, η and size reduction for the 6-element array of the slot antennas compared with that of the printed dipole. The directivity is approximately 11 dB, and the efficiency is 91.39 % for the printed dipole, 83.25 % for the CPA, 82.49 % for the slot dipole and 81.78 % for the bow-tie. The slot antenna arrays achieve size reduction relative to the printed dipole array ranging from 12 % for the bow-tie, 24 % for the slot dipole and 28 % for the CPA. The size reduction is based on the total length of the 6-element array relative to that of the printed dipole array. The total length is calculated as [6×*Wa*+5×*ds*], where W_a is the width of the antennas, which equals to *W* for all antennas except the CPA. For the CPA, this length is *W*+2×*S2*, and d_S is the separation distance between the antennas.

Radiation patterns are calculated for 6-element array. The radiation pattern in *x-y* plane is shown in Fig. 21 for the slot antennas, while there is no radiation in the *x-y* plane by the printed dipoles. The co-polar and cross-polar radiation patterns in *x-z* and *y-z* planes are shown in Figs. 22 and 23, respectively. As shown in the *x*-z plane, the cross-polarization is less than –40 dB in the printed and slot dipole, -34 dB in the CPA, and –27 dB in the bow-tie where E_θ is the co-polar component in the printed dipole and E_ϕ is the co-polar in the slot dipoles. As shown in *y*-z plane, the cross-polar level is less than –40 dB for all antennas where E_ϕ is the co-polar component in the printed dipoles and E_θ is the co-polar in the slot antennas. Figure 24 shows the 3-dimension radiation pattern for all antennas. It is clear that the side lobe levels are higher in the printed dipole relative to those patterns of the slot antennas, which is not a desirable characteristic for phased antenna array system.

Table 3. Radiation properties for 6-element array.

	BW (%)	*D (dB)*	η *(%)*	*Reduction*
Printed dipole	12.5 %	11.28	91.39	0 %
Slot dipole	21.5 %	10.45	82.49	24 %
CPA	17.0 %	10.33	83.25	28 %
Bow-tie	40.0 %	10.65	81.78	12 %
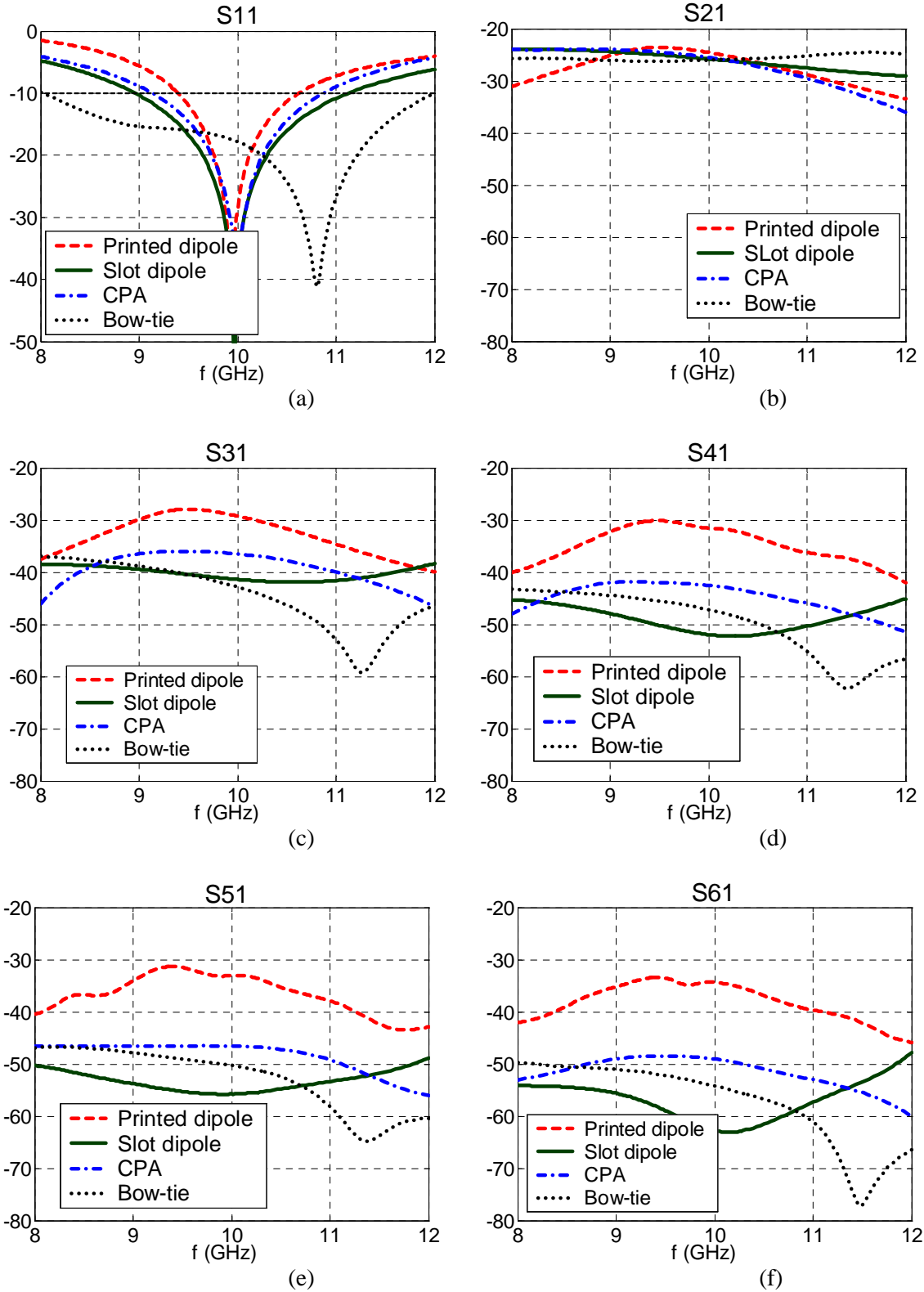
Fig. 20. Return loss and coupling between elements of 6-element array module for printed dipole, slot dipole, CPA and bow-tie slot antenna with distance between elements equals to 20.8, 3, 8.5, and 4 mm, respectively. (a) S11, (b) S21, (c) S31 (d) S41, (e) S51 and (f) S61.
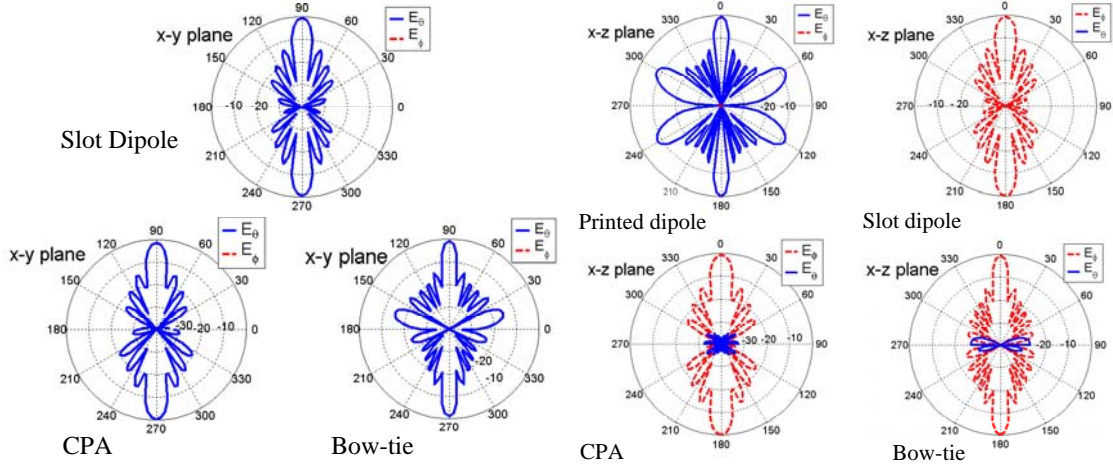
Fig. 21. Radiation pattern in x-y plane.

Fig. 22. Radiation pattern in x-z and y-z planes.
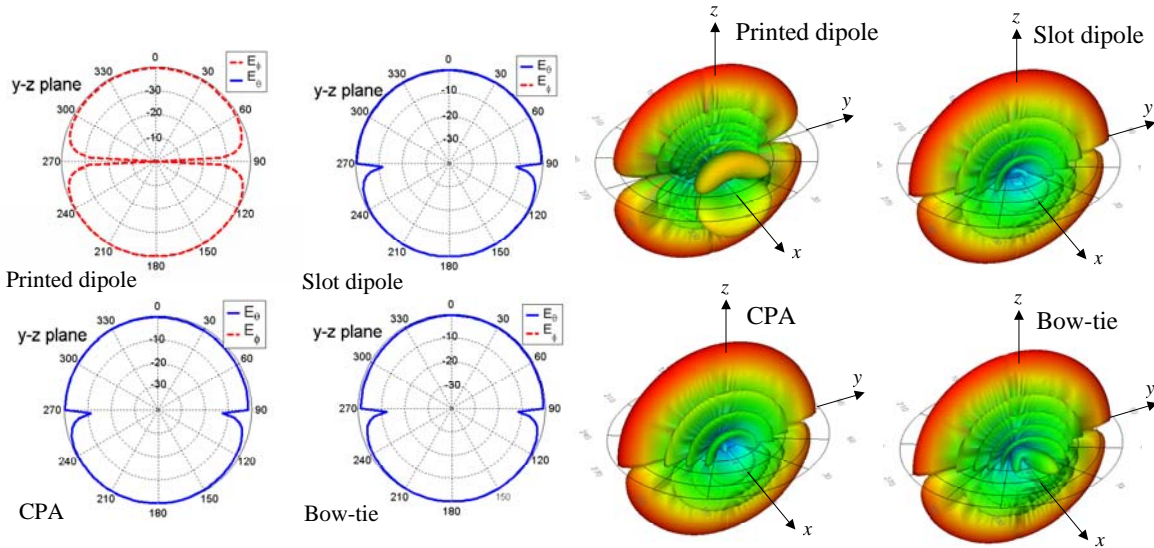
Fig. 23. Radiation pattern in x-z and y-z planes.

Fig. 24. Total 3D radiation pattern.

V. CONCLUSIONS

In this paper, a printed dipole antenna and three microstrip slot antennas operating at 10 GHz in the X-band (8-12 GHz) are presented. Parametric studies for each antenna showing the effect of each geometrical parameter and antennas' dimensions in terms of λ_g are presented. Slot antennas achieve better BW that reaches 52% for the bow-tie slot antenna. In addition, the arrays of slot antennas are smaller and have less than –24 dB coupling between elements as obtained for the 6-element arrays. The efficiencies of the slot antennas are near 80%, slightly less than the printed dipole antenna. The cross-polarization level is less than –27 dB in the *x-z* plane and –40 dB in the *y-z* plane. All antennas show good radiation pattern stability over the entire band of operation.

REFERENCES

[1] K-L. Wong, Compact and Broadband Microstrip Antennas, New York, NY, *John Wiley and Sons,* 2002.

[2] K. Li, C. H. Cheng, T. Matsuni and M. Izutsu, "Coplanar patch antennas: principal, simulation and experiment," *Proc. Antennas Propagat. Soc. Int. Symp.*, Boston, MA, vol. 3, pp. 402-405, July 2001.

[3] K. F. Tong, K. Li, T. Matsuni and M. Izutsu, "Wideband coplanar waveguide fed coplanar patch antenna," *Proc. Antennas Propagat. Soc. Int. Symp.*, Boston, MA, vol. 3, pp. 406-409, July 2001.

[4] A. Z. Elsherbeni, Abdelnasser A. Eldek, B. N. Baker, C. E. Smith and K-F Lee, "Wideband coplanar patch-slot antennas for radar applications," *Proc. Antennas Propagat. Soc. Int. Symp.*, Houston, TX, vol. 2, pp. 436-439, June 2002.

[5] Yu-De Lin and Syh-Nan Tsai, "Coplanar waveguide-fed uniplanar bow-tie antenna," *IEEE Trans. Ant. Prop.*, vol. AP-45, no. 2, pp. 305-306, Feb. 2000.

[6] A. A. Eldek, A. Z. Elsherbeni, C. E. Smith and K-F Lee, "Wideband slot antennas for radar applications," *Proc. IEEE Radar Conf.*, Huntsville, AL, pp. 79-84, May 2003.

[7] E. A. Soliman, S. Berbels, P. Delmotte, G. A. E. Vandenbosch, and E. Beyne, "Bow-tie slot antenna fed by CPW," *Electron Lett.,* vol. 35, pp. 514-515, 1999.

[8] Jen-Fen Huang, Chih-Wen Kuo, "CPW-fed bow-tie slot antenna," *Microwave Opt. Technol. Lett.*, vol. 19, no. 5, pp. 358-360, Dec. 1998.

[9] M. Miao, B. L. Ooi, P. S. Kooi, "Broadband CPW-fed wide slot antenna," *Microwave Opt. Technol. Lett.*, vol. 25, no. 3, pp. 206-211, May 2000.

[10] A. A. Eldek, A. Z. Elsherbeni and C. E. Smith, "Wideband bow-tie slot antennas for radar applications," *2003 IEEE Topical Conference on Wireless Communication Technology,* Honolulu, Hawai, October 2003.

Call for Papers

The Applied Computational Electromagnetics Society

Announces a Special Issue of the ACES Journal on:

Review of Computation and Modeling Techniques for Phased Array Antennas

The Applied Computational Electromagnetics Society is announcing the new Special Issue of the ACES Journal dedicated to the topic of Review of **Computation and Modeling Techniques for Phased Array Antennas.**

Phased array antennas have unique capabilities that enhance the performance of all **military** and **commercial** communication systems, of **remote sensing radar** systems, and some recent, innovative **biomedical** applications. The most fundamental requirement for attaining a cost-effective design and development of such antenna systems is, however, the ability of very rapidly predicting the system performance, already in the early phases of the design process, much ahead of any prototype fabrication. A continuous ongoing review and re-evaluation of state-of-the-art computational techniques, performed with the intent of *pushing the envelope*, has clearly shown fundamental limitations of current phased-array antenna performance-prediction capabilities. Fortunately however, the recognition of current limitation stimulates new, more advanced developments in the methods of computer analysis and design of phased arrays.

The Guest Editors of this Special Issue of the ACES journal solicit the submission of papers that re-evaluate the capabilities of current commercially-available, established, state-of-the-art Computer Simulation Codes, such as NEC, SuperNEC, HFSS, ENSEMBLE, IE3D, FIDELITY, NECBSC, NEWAIR, AAPG and similar, particularly those that are being routinely used to analyze the performance of Phased Array Antennas System characterized by a wide range of different architectures. In addition, application of these commercially available software to the performance modeling of phased arrays for biomedical applications shall receive special attention.

In keeping with the established ACES objectives and interests, the validation of the results computed from any of the available computer simulation codes, attained by verifying the simulation results from appropriate measurements, and against *existing* theoretical formulations of canonical problems, are strongly encouraged.

In contrast, papers that describe **NEW hardware design** or **theoretical analysis**, for phased arrays, are **deemed beyond the scope of this ACES special issue**. The Proceedings of the IEEE International Symposium on Phased Array Systems and Technology (1996, 2000 and 2003), and the special issue of IEEE AP Trans. on Phased Arrays (March 1999), that cover a broader range of topics, are considered more appropriate for such submissions, than the here announced special issue of the ACES Journal.

This special issue of the ACES Journal solicits papers that describe original work, relating to both planar and conformal arrays, and in particular to conformal arrays mounted on surfaces with variable and double curvatures, and flush-mounted on biological (humans etc.) media and other novel environments.

11 March 2004

The following list, is an attempt at suggesting a number of open issues, that are still largely unresolved in the computer simulation of phased array performance:

- What is the maximum electrical size of a planar array that can be analyzed using the present CAD tools?
- What type of conformal arrays on non-canonical, convex surfaces can be analyzed using the present CAD tools? (Arrays flush-mounted on biological media are also included here.)
- What are the required computational resources, and the actual solution speed attained by the above CAD tools?
- How can the accuracy of the solution be determined, and what kind of physical validation is appropriate to verify the currently available CAD tools?
- What are the limitations of the algorithms currently used in the codes, in predicting the element-to-element mutual coupling, the active-element pattern, and radiation patterns of a complete phased array?

Prospective authors are encouraged to submit papers that cover the above-mentioned issues, and focus on the topics listed here below:

Suggested Topics:

1. Impact of element coupling on (finite) array performance parameters.

2. Evaluation of edge diffraction effects, and their reduction techniques.

3. Application of Multi-Level Fast-Multipole Methods (MLFMM) to array problems.

4. Beam-steering with reduced number of expensive steering controls.

5. Correlation between beam steering, element impedance and matching.

6. Design and performance modeling of multi-port matching networks.

7. Synthesis of aperture distributions for high-directivity phased arrays.

8. Modeling of arrays on canonical and non-canonical convex surfaces.

9. For planar and conformal phased arrays with *__wideband__* elements – the effects of: 1. ground plane size and shape (planar), and, 2. principal radii of curvatures (conformal), on beam-steering, gain, polarization and impedance bandwidths.

10. Validation of predictions obtained from CAD software against measured data and/or existing theoretical formulations.

TENTATIVE DEADLINE FOR SUBMISSION PAPERS IS November 15, 2004

Potential contributors wishing to discuss the suitability of their contribution may contact either of the Guest Editors listed below. Please upload your manuscript to the ACES server at **http://aces.ee.olemiss.edu** by using the "upload" button, "Journal", "upload a new paper", then select "special issue by Dr. Chatterjee and Dr. Speciale". The review process will begin as the editor finds your paper(s) on the ACES web site. **Email or paper submission is not accepted.**

Professor Deb Chatterjee *CSEE Division, UMKC* *Tel.: (816)235-1276 (work)* *e-mail: chatd@umkc.edu*	*Dr. Ross A. Speciale* *Research & Development, Inc.* *Tel.: (925)335-9385 (work)* *e-mail: rspeciale@comcast.net* *Home Page: http://home.comcast.net/~rspeciale/*
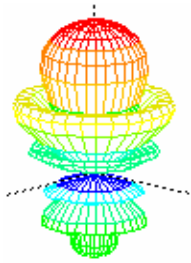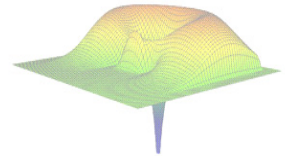
11 March 2004

The 20th Annual Review of Progress in Applied Computational Electromagnetics, April 19-23, 2004

Sheraton Syracuse University Hotel and Conference Center Syracuse, New York

The 20th Annual Review of Progress in Applied Computational Electromagnetics Symposium will be held in the Sheraton Syracuse University Hotel and Conference Center in Syracuse, New York. The Sheraton hotel will accommodate all the technical sessions on the same floor and the lodgings for all the attendees. It is an ideal opportunity to participate in a large gathering of EM analysis enthusiasts. The purpose of the Symposium is to bring developers, analysts, and users together to share information and experience about the practical application of EM analysis using computational methods. The symposium offers more than 150 technical presentations of all aspects of electromagnetic computational analysis and applications. The technical presentations will be offered on Monday to Thursday in two parallel sessions in the morning and afternoon. Short courses will be offered on Sunday April 18, and on Friday April 23. A **$500** prize will be awarded to the authors of the best non-student paper presented (poster or oral) at the 20th Annual Review. Papers will be judged by the ACES prize-paper committee. Additionally, the best three (**3**) student papers presented at the 20th Annual Review will be announced at the symposium banquet. Student papers submitted for this competition will be judged by three (3) members of the ACES Board of Directors. The first, second, and third winners will be awarded cash prizes of **$300, $200**, and **$100**, respectively.

The Sheraton Hotel is located at 801 University Avenue, Syracuse, New York 13210. For reservation, call (315) 475-3000 and mention the **Meeting Code : 4162** . For any additional information, including travel and lodging, please contact the conference Chair: **Tapan K. Sarkar (tksarkar@syr.edu, Tel: 315-443-3775, Fax: 315-443-4441)**, or visit ACES web site at: http://aces.ee.olemiss.edu

The latest conference agenda is available at ACES site. It is recommended to check the site regularly for last minutes updates.

ACES 2004

The 20th Annual Review of Progress in Applied Computational Electromagnetics

PRELIMINARY AGENDA

Syracuse University
April 19-23, 2004

Symposium Chair: **Tapan K. Sarkar**

Symposium Co-Chair: **Atef Elsherbeni**

Symposium Administrator: **Richard W. Adler**

Short Course Chair: **John Shaeffer**

Exhibits Chair: **Andrew L. Drozd**

Publicity Chair: **Omar M. Ramahi**

Feb 11, 2004

Sessions

	Session Title	Papers	Chair
1	**Applications of FEKO**	**8**	
2	**Electromagnetic Modeling**	**10**	
3	**Computational Techniques**	**10**	
4	**Advanced Computational Techniques for Antenna Design**	**10**	
5	**High-Speed Interconnects: modeling and simulation**	**6**	
6	**Black Box Modeling**	**5**	
7	**Optimization of Complex EM problems**	**9**	
8	**Electromagnetic Applications for the DoD**	**10**	
9	**FDTD and Applications**	**10**	
10	**Advances in CEM**	**8**	
1	**Advances in Finite-Difference Time Domain Modeling**	**10**	
12	**Recent Advances in Time Domain Modeling Techniques**	**10**	
13	**Smart Antennas and Computational Electromagnetics**	**10**	
14	**Bianisotropic and Metamaterial**	**10**	
15	**Higher Order Methods**	**10**	
16	**Electromagnetic Modeling Using WIPL-D Code(I)**	**10**	
17	**Electromagnetic Modeling Using WIPL-D Code(II)**	**8**	

Regular Sessions Overview By Day

Date	AM		PM	
	Session I	Session II	Session I	Session II
Mon	8:05 opening Remarks 8:10-9:50 (4) break 10:20-12:00 (4) **Application of FEKO (8)**	8:05 opening Remarks 8:10-9:50 (4) break 10:20-12:20 (6) **Electromagnetic Modeling (10)**	1:25 opening Remarks 1:30-2:50 (4) break 3:20-5:20 (6) **Bianisotropic and Metamaterial (10)**	11:25 opening Remarks 1:30-2:50 (4) break 3:20-5:20 (6) **Advances in Finite-Difference Time Domain Modeling (10)**
Tue	8:05 opening Remarks 8:10-9:50 (4) break 10:20-12:20 (6) Computational Techniques (10)	8:05 opening Remarks 8:10-9:50 (4) break 10:20-12:20 (6) **Advanced Computational Techniques for Antenna Design (10)**	1:25 opening Remarks 1:30-2:50 (4) break 3:20-5:40 (7) **Black Box Modeling (5) High-Speed Interconnects: modeling and simulation (6)**	1:25 opening Remarks 1:30-2:50 (4) break 3:20-5:20 (6) **Smart Antennas and Computational Electromagnetics (10)**
Wed	8:05 opening Remarks 8:10-9:50 (4) break 10:20-12:20 (6) **Electromagnetic Modeling Using WIPL-D Code(I) (10)**	8:05 opening Remarks 8:10-9:50 (4) break 10:20-12:20 (6) **Recent Advances in Time Domain Modeling Techniques (10)**	1:25 opening Remarks 1:30-2:50 (4) break 3:20-5:20 (4) **Electromagnetic Modeling Using WIPL-D Code(II) (8)**	1:25 opening Remarks 1:30-2:50 (4) break 3:20-5:20 (4) **Advances in CEM(8)**
Thu	8:05 opening Remarks 8:10-9:50 (4) break 10:20-12:20 (6) **Higher Order Methods (10)**	8:05 opening Remarks 8:10-9:50 (4) break 10:20-12:20 (6) **Electromagnetic Applications for the DoD (10)**	1:25 opening Remarks 1:30-2:50 (4) break 3:20-5:20 (6) **FDTD and Applications (10)**	1:25 opening Remarks 1:30-2:50 (4) break 3:20-5:00 (5) **Optimization of Complex EM problems (9)**

List of Papers by Session

1. Applications of FEKO (8)

Paper #	Author	Title
904175	Ulrich Jakobus	Overview of Recent Extensions in the Electromagnetics Computer Code FEKO and their Application
92004100477	James S. Turner	Modeling the New Arecibo Dual Band High Frequency (HF) Facility
904136	Averty Florent	Characterization of focusing properties of a homogeneous lens and design of its primary source with software
904162	Masanobu Hirose	Antenna Pattern Comparison of a Microstrip Antenna on a Finite Substrate Using Near-Field Measurement and FEKO
904269	FJC Meyer	Introducing the Finite Element Method into the Commercially Available
904177	C. Babu Ravipati	Analysis and Design of Broad-band and Multi-frequency Antennas using FEKO
904252	Mazen K. Alsliety	A Comparative Study of Different Methods for Computing Circular Polarization Gain
904182	Nickolai Zhelev Kolev	Design of a Microstrip Conform GPS Patch Antenna

2. Electromagnetic Modeling (10)

Paper #	Author	Title
92004100465	Surendra Singh	Application of an iterative method for the solution of electromagnetic scattering from wire antennas
904284	Ehab K. I. Hamad	A Proposed pi-Structure RF MEMS Switch for Wide Bandwidth and High Isolation Applications
904295	Giuseppe Conciauro	Planar Model of RF MEMS Shunt-Capacitive Switches
904301	Alexander B. Yakovlev	Electric Dyadic Green's Function for an Ideal Hard Surface Circular Waveguide
904166	BAGHAI-WADJI, Alireza	On the Factorization of Potential Functions without Utilizing the Addition Theorem
904171	BAGHAI-WADJI, Alireza	Analysis of Electromagnetic Waves in Axially-periodic Structures in Cylindrical Co-ordinates
904272	M. T. Buber	Non-constant speeds of light in vacuum
904248	Steven R. Best	A Comparison of the Quality Factors of Impedance Matched
904223	Steven R. Best	Modeling a Slotted Multiband Gasket Monopole Antenna Using NEC
904312	Magdy F. Iskander	New Ray-Tracing Techniques and Propagation Modeling for Challenging Communication Environments

3. Computational Techniques (10)

Paper #	Author	Title
904207	Jason D Morsey	A broadband, low storage preconditioning scheme based on reduced coupling for full-wave method of moments solvers
92004100466	Guowei Wei	A wavelet-collocation approach for computational electromagnetics
92004100467	Guowei Wei	A wavelet-collocation method for solving the Helmholtz equation with high wavenumbers
904233	Debalina Ghosh	Hybrid Method for the Generation of Wideband Electromagnetic Response for Composite Bodies
904228	YUNHUI CHU	Large-Scale Computation for Low-Frequency Problems
904193	Keli Sun	Fundamental Mode Approach to Forward Problem Solutions in EMI Scattering ---- Inferring fundamental solutions from training data
904183	Branislav M. Notaros	Higher Order Geometrical Modeling and Higher Order Field/Current Modeling in FEM, MoM, and PO Simulations
904285	Ayan Kumar Bandyopadhyay	Improving the Numerical Efficiency of Generalized Multipole Technique by Non-redundant Multipole Choices
904238	B. Shanker	Fast multipole augmented analysis of scattering from dielectric objects using the single integral equation
904299	Baek Ho Jung	Analysis of Scattering from Three-Dimensional Conducting Bodies Coated with a Dielectric Material

4. Advanced Computational Techniques for Antenna Design (10)

Paper #	Author	Title
904114	Andreas Rennings	A compact single/dual-band printed inverted-F type antenna structure
92004100469	Antonije Djordjevic	Rigorous analysis of coaxially-fed collinear arrays
904201	Atef Elsherbeni	Wideband Bow-Tie Slot Antennas with Tapered Tuning Stubs
904106	Kazuhiro Hirasawa	A Broadband Flat Dipole Antenna with an Asymmetrical Feed
92004100463	LI Long	A Progressive Numerical Method Combined with MoM for a Fast Analysis of Slot Antenna Array
904108	Manju Paulson	Computer-Aided Design of Dual Frequency Arrow shaped Microstrip Antenna
904105	Pasi Ylä-Oijala	Analysis of Microstrip and Patch Antennas by the Method of Moments and RWG Basis Functions
904203	Vicente Rodriguez	DESIGN OF A NEW BROADBAND DOUBLE RIDGE GUIDE HORN FOR ELECTROMAGNETIC COMPATABILITY TESTING HAVING A SINGLE MAIN LOBE
904273	Serhend Arvas	GROUP VELOCITY FOR AN IDEAL DIPOLE
92004100470	Antonije Djordjevic	Multiband modem antenna for cellular networks

5. High-Speed Interconnects: modeling and simulation (6)

Paper #	Author	Title
904213	Dharmendra Saraswat	Fast Passive Macromodeling of S-parameter based Interconnect Subnetworks
904214	Emad Gad	Analysis of Frequency Dependent Transmission Lines Using Integrated Congruence Transform
904245	Hideki Asai	A Model Order Reduction Technique for Hybrid Systems Composed of Electromagnetic Systems and Lumped RLC Circuits
904222	JIFENG MAO	Electromagnetic Modeling of On-chip Power Distribution Networks
904271	Kausik Chatterjee	A Novel Stochastic Algorithm For The Extraction Of Frequency-Independent Partial Inductances In Digital IC Interconnect Structures And A Frequency-Dependent Generalization
904244	Q.J. Zhang	Application of Neural Networks for High-Speed VLSI Interconnects Modeling and Design

6. Black Box Modeling (5)

Paper #	Author	Title
904231	Bhyrav Mutnury	Black-Box Modeling of Non-Linear I/O Drivers
904293	Jilin Tan	Via Modeling in Multi-Gbits/s Signal Analysis
904216	Shahrooz Shahparnia	Ultra Wide-Band Electromagnetic Interference (EMI) Reduction from Printed Circuit Boards (PCB)
904239	Stefano Grivet-Talocia	Passive time-domain macromodeling of large complex interconnects
904287	Yidnekachew S. Mekonnen	Improved High-Order Rational Approximation by Combining Rational Interpolation with the Vector Fitting Method

7. Optimization and Solution of Complex EM problems (9)

Paper #	Author	Title
904296	Atef Elsherbeni	Bayesian Optimization Techniques For Antenna Design
904235	Jie Yang	Reconstructing of a Non-Minimum Phase Response from Far-Field Power Pattern of an Electromagnetic System
904261	Mohamed Bakr	Efficient Adjoint Sensitivity Estimation for Time-Domain Techniques with Structured Grids
904274	NATALIA K. NIKOLOVA	Response Sensitivity Analysis with Frequency-Domain Full-Wave Electromagnetic Solvers
904243	Q.J. Zhang	Automatic Neural Network Model Generation for EM Modeling of Embedded Passives in Multi-layer Printed Circuits
904217	Shahrooz Shahparnia	Design Considerations for High-Impedance Surfaces Embedded in Printed Circuit Boards
904208	Deb Chatterjee	Optimization Studies for Single-Layer, Wideband, U-Slot Antennas on Microwave Substrates Using the IE3D Code
92004100474	Senglee Foo	On solving method-of-moments matrix using sparse matrix technique
92004100460	Mehmet K. Ozdemir	Realistic Head Modeling for the Inverse Problem of Electromagnetic Source Imaging of Brain Using FEM

8. Electromagnetic Applications for the DoD (10)

Paper #	Author	Title
904102	Andrew D. Greenwood	Hybrid Modeling of Electromagnetic Plasmas
904186	Fridon Shubitidze	A new numerical procedure for efficient and accurate representation of low frequency EM responses for a heterogeneous object
904194	Jonathan E. Luminati	Fourier Transform and Back-Projection Methods of SAR/ISAR Imaging Using Circumscribed Processing Regions
904242	Leo Kempel	Calibrated Modeling of Material Measurements
904240	Ray Ko	Modeling eddy current crack detection in multi-layer airframe structures using the volume-integral method
904200	Stanley Kubina	Modeling Multiple HF Antennas on the C-130/Hercules Aircraft - Part I
904178	Stephen Gedney	High-Order Locally Corrected Nyström Solution with Mixed-Order Basis Functions for Electromagnetic Scattering
904204	Michael E. McKaughan	USCG 270' Cutter - NVIS Antenna Study
904282	Daniel Faircloth	A Finite Element Method for the Electromagnetic Characterization of Quasi-Magnetostatic Problems Found in UXO Detection and Discrimination
904246	Andre BARKA	Modal expansion functions combined with EFIE applied to Air Intake / Engine RCS applications

9. FDTD and Applications (10)

Paper #	Author	Title
904294	Ahmed A. Kishk	ASYMPTOTIC STRIP BOUNDARY CONDITION IN THE FINITE DIFFERENCE TIME DOMAIN METHOD
904286	Atef Elsherbeni	FDTD Formulations for Scattering from Three Dimensional Chiral Objects
904173	Chen Wu	Computing Far Field Impulse Response of a 54-Element Waveguide Slot Array Using FDTD Method
92004100475	Edward Lule	Analysis using the FDTD method of the Properties of Koch Island Fractal on an Ultra Wideband Bowtie Dipole Antenna
904156	Hossam A Abdallah	An Optimized high-order implicit FDTD solver with One-sided TF/SF for simulation of photonic devices
92004100476	Michiko Kuroda	Numerical Analysis of MEMS-Based Variable Capacitors Involving the Combined Effect of Mechanical and Electrical Forces
92004100464	Ming Zhang	Analysis of Portable Radios (850 &1900MHz) with Hand-Free Kits FDTD and Applications
904195	Qiubo Ye	Investigation of Feed Gaps of UWB Microstrip Dipole Antennas and FDTD Simulation
904163	Yotka Rickard	Off-Grid Perfect BCs for the FDTD Method
904170	P. Mohanan	Time Domain Analysis of a Microstrip Line Excited Compact Rectangular Dielectric Resonator Antenna

10. Advances in CEM (8)

Paper #	Author	Title	
904297	Osama Mohammed	Wavelet Analysis of Permanent Magnet Synchronous Machine Flux Density Harmonic Content With Different Pole Number Designs	
904107	Rensheng Sun	Electromagnetic Modeling of an Adaptable Multimode Microwave Applicator for Polymer Processing	S
904151	Ross A. Speciale	The Tilted-Ellipse Representation of Standing-Wave Patterns.	
904303	Luis E. Garcia-Castillo	A Novel 3D Hybrid FEM-PO Technique for the Analysis of Scattering Problems	
904197	Robert J. Bonneau	B-Spline Wavelet Basis Models For Improved Radar Detection	
904122	Randy L. Haupt	Selecting Genetic Algorithm Operators for CEM Problems	
904289	Deb Chatterjee	Effect of Substrate Permittivity and Thickness on Performance of Single-Layer, Wideband, U-Slot Antennas on Microwave Substrates	
904298	Baek Ho Jung	Transient Electromagnetic Scattering from Dielectric Objects Using Time-Domain Integral Equation	

11. Advances in Finite-Difference Time Domain Modeling (10)

Paper #	Author	Title
904147	Andreas Rennings	An efficient operator based implementation of a wavelet-transformed FDTD scheme
92004100468	Guowei Wei	High-order FDTD methods via derivative matching for electromagnetic computation involving material interfaces
904164	Hossam A Abdallah	Simple Dispersion Analysis of 2nd and 4th order FDTD Schemes
904110	Michal Wiktor	Discrete projection for Finite Difference methods
92004100481	Mikko Kärkkäinen	FDTD Implementation of Impedance Sheet Conditions for Parallel Wire Arrays
904113	Oliver Pertz	Improved EM Field Simulation with a Novel Wavelet-Based Method
904206	Qunsheng Cao	Studies of Bi-static Scattering of Arbitrary Targets using Multiresolution Time Domain
904112	Thomas Bolz	Consideration on the Mutual Coupling Impedance Network
92004100461	Zhou Weihong	Analysis of Time-Domain Scattering Field in Soil and Cube Underground With 2-D FDTD
92004100472	Kian Paran	FDTD Simulation of Electromagnetic Radiation from Monopoles on Spherical-Lossy Earth

12. Recent Advances in Time Domain Modeling Techniques (10)

Paper #	Author	Title
904104	Changning Ma	On the Complex Envelop FDTD Method
92004100473	Christophe Fumeaux	FVTD Simulation of a Probe-fed Hemispherical Dielectric Resonator Antenna with Finely Resolved Structural Details
904190	John Paul	Time-Domain Simulation of Chaotic Dynamics in Nonlinear Frequency-Dependent Dielectric Materials
904181	Dzianis Lukashevich	Shift-Inverse Technique in TLM-ROM
904209	Gaetano Marrocco	Combining data-fitting and signal processing for efficient time-domain characterization of aperture antennas
904300	José Represa	PML Absorbing Boundary Conditions For Multi-Resolution Time-Domain Techniques Based On The Discrete Wavelet Transform
904168	Luca Pierantoni	Full-Wave Analysis of Integrated Optical Components by the TLMIE Method
904198	Petr Lorenz	Definition of Radiation Field Boundary Conditions for Spherical Simulation Domain in Time-Domain Methods
904254	Q.J. Zhang	Time-Domain Neural Network Modeling Approaches for Embedded Passives in Multilayer Printed Circuits
904257	Zhong Ji	A Stable Solution of Time Domain Electric Field Integral Equation for Conducting Bodies Using the Laguerre Polynomials

13. Smart Antennas and Computational Electromagnetics (10)

Paper #	Author	Title
92004100479	FRANCESCO ZIRILLI	MATHEMATICAL MODELS OF SMART OBSTACLES IN ELECTROMAGNETIC SCATTERING
904165	Ramesh K. Pokharel	Analysis of DSRC Electromagnetic Environment on Express Highway Installed with Wave Absorbers
904236	Raul Fernandez-Recio	Estimation of DOA for Different Frequencies using an Interpolation Technique
904196	Raviraj Adve	Minimum Norm Mutual Coupling Compensation for MUSIC-based Direction of Arrival Estimation
904230	Santana Burintramart	Multiple Frequency Parametric Target Location using Matrix Pencil Method
904229	Santana Burintramart	Estimation of the Two-Dimensional Direction of Arrival by The Diagonal Matrix Pencil Method
904226	Seunghyeon Hwang	Error Bound due to the Random Position Errors in Adaptive Processing Using a Nonuniformly Spaced Array
904268	Shengchun Zhao	Interference Suppression via Frequency Domain Principal Component Analysis Method
904225	Wonsuk Choi	Amplitude-only Space–Time Adaptive Processing (STAP) based on Deterministic Least-Squares Approach
904221	Emmanuel H. Van Lil	Theoretical Investigations and Broadband Experimental Verification of the time-domain SAGE DOA algorithm

14. Bianisotropic and Metamaterial (10)

Paper #	Author	Title
904232	Alkim Akyurtlu	Analysis of the Interaction of Electromagnetic Waves with a Chiral Cylinder using a Novel FDTD Approach
904184	Ana Grande	Analyzing the stability of the new FDTD technique for the non-dispersive bi-isotropic media using the von Neumann method
92004100480	Ari Sihvola	Modeling of metamaterials with classical homogenization principles
904202	Jay K. Lee	Dispersion Characteristics of Conductor-backed Coplanar Waveguide on an Anisotropic Substrate
904278	Mehmet Yuceer	Solution of RCS of a Chiral BOR
92004100482	Mikko Kärkkäinen	FDTD Simulations of Wave Propagation in Anisotropic Backward-Wave Slabs
904137	Mohammed M. Bait Suwailam	Simulation of Lorentzian DNG materials Using FDTD Method and Z-transform
904176	Rafael R. Boix	Full-wave spectral domain analysis of microstrip circuits and antennas fabricated on magnetized ferrites
904111	Natalya I. Manaenkova	ANALYSIS OF SOLITON PULSE ENVELOPE IN A NONLINEAR MEDIUM
92004100478	Nobel Mathew	Optimization of a Circularly Polarized Single-Feed UHF Patch Antenna on a Nanosatellite Metal Platform

15. Higher Order Methods (10)

Paper #	Author	Title
904291	Aly E Fathy	Circular Ring E-Plane Element Pattern Integral Representation and its Asymptotic Evaluation
904262	Elizabeth Bleszynski	Application of wavefront and ray tube evolution methods in the development of a high frequency algorithm with asymptotically frequency independent complexity
904174	Fernando Reitich	A new high-order high-frequency integral equation method for the solution of scattering problems. II: Multiple-scattering configurations
904224	Mengtao Yuan	The analysis of transient scattering for rectangular incident waves using the discrete Laguerre transforms
904152	Oscar P. Bruno	A new high-order high-frequency integral equation method for the solution of scattering problems I: Single-scattering configurations
904146	Paul Hussar	High Frequency Radiation Pattern Analysis for Antennas Mounted on Material-Coated Conducting Platforms of General Shape
904263	Shinichiro Ohnuki	Monte Carlo Simulation of Rough Surface Scattering Problems on Comparison among Various Methods
904218	Kausik Chatterjee	A Floating Random-Walk Solution for the Transverse Magnetic Electromagnetic Problem: A Homogeneous Benchmark
904247	Luca Perregrini	A Perturbational Technique for the Fast Modeling of Printed Reflectarray Elements
904260	Yuriy Shlepnev	Scattering matrix descriptors of Trefftz finite elements

16. Electromagnetic Modeling Using WIPL-D Code(I) (10)

Paper #	Author	Title
904270	Atef Elsherbeni	Design of Wideband Printed Monopole Antenna Using WIPL-D
904280	DENIAU Virginie	Optimization of Three-dimensional TEM cell for Electromagnetic Compatibility Testing
904249	Dragan I. Olcan	Precise and Efficient EM modeling of Trees with WIPL-D Code
904304	Wayne Kim	Novel High Performance Low Cost Phase Shifters Design Based on the Ferroelectric Materials Technology Using the WIPL-D Code
904256	Hossam Ahmed Abdallah	Comparison of return loss calculations with measurements of narrow-band microstrip patch antennas
904250	Mitsuo Taguchi	Numerical analysis of microstrip antenna by using electromagnetic simulators
904279	Ralf Klukas	Dual State Resonator Design for Plasma Ignition by Means of Microwave Energy
904227	Reddy Vangala	Modeling of Ceramic Filters Using WIPL-D
904259	Ronald H Johnston	MICROSTRIP LINE JUNCTIONS -A Comparison of WIPL-D Simulations and Measured Data
904253	Tasic Miodrag	Full 3D EM Modeling of Yagi Antenna for WLAN

17. Electromagnetic Modeling Using WIPL-D Code(II) (7)

Paper #	Author	Title
904275	Christopher Card	Development of a Parallel Scene Generation Electromagnetic Modeling Tool
904220	Eric Mokole	Preliminary Calculated Scatter from Trihedral Corner Reflector with WIPL-D
904288	Harvey K. Schuman	Array Antenna Design with WIPL-D
904267	Robert W. McMillan	Comparison of WIPL-D to Other EM Computation Methods
904276	Saad Tabet	Alpha Test Analysis of WIPL-DP
904241	Hany E. Yacoub	Investigation of a Forward Looking Conformal Broadband Antenna for Airborne Wide Area Surveillance
904311	Mary Cannella Taylor	Metallic vs. Dielectric Modeling in WIPL-D
904313	Michael Simcoe	Low-frequency Synthetic Aperture Radar Imaging of Complex Scenes using Numerical Electromagnetic Analysis

ADVERTISING RATES

	FEE	PRINTED SIZE
Full page	$200	7.5" × 10.0"
1/2 page	$100	7.5" × 4.7" or 3.5" × 10.0"
1/4 page	$50	3.5" × 4.7"

All ads must be camera ready copy.

Ad deadlines are same as Newsletter copy deadlines.

Place ads with Ray Perez, Newsletter Editor, Martin Marietta Astronautics, MS 58700, PO Box 179, Denver, CO 80201, USA. The editor reserves the right to reject ads.

DEADLINE FOR THE SUBMISSION OF ARTICLES

Issue	Copy Deadline
March	February 1
July	June 1
November	October 1

For the *ACES NEWSLETTER*, send copy to Bruce Archambeault in the following formats:

1. A PDF copy.
2. A MS Word (ver. 97 or higher) copy. If any software other than WORD has been used, contact the Managing Editor, Richard W. Adler **before** submitting a diskette, CD-R or electronic file.

Last Word

Reality is merely an illusion, albeit a very persistent one..
----Albert Einste